ALMA MATER STUDIORUM - UNIVERSITÀ DI BOLOGNA

CAMPUS DI CESENA

DIPARTIMENTO DI

INGEGNERIA DELL'ENERGIA ELETTRICA E DELL'INFORMAZIONE
"GUGLIELMO MARCONI"

CORSO DI LAUREA IN INGEGNERIA BIOMEDICA

ELECTROSPUN SCAFFOLDS FOR REGENERATION OF
MUSCULOSKELETAL INTERFACE TISSUES

Elaborato in
BIOMATERIALI

Relatore:

Prof. Ing. Luca Cristofolini

Presentata da:

Gabriele Massafra

Co-relatori:

Prof. Ing. Andrea Zucchelli

Dott. Alberto Sensini

Ing. Carlo Gotti

Sessione II
Anno Accademico 2019-2020

Abstract

The musculoskeletal system is composed by muscular, articular and bony structures. These tissues are very different from each other and have a wide disparity in mechanical properties, a gradual transition from one tissue to the other one is therefore necessary to avoid the concentration of stresses at the junction site. Fortunately, evolution led to the development of particular interfaces, which are specific structures that allow the right transmission of the load distributing them on a wider area over the junction. The interfaces connected to the bones are called entheses and this review will focus on those between tendons/ ligaments and bone. This thesis will also cover the myotendinous junction, i.e. between muscle and tendon. Numerous tissue injuries can affect muscles, bones, tendons or ligaments and several times, the injury occurs at the junction. When this happens, there are several possibilities to go through, each with their advantages and drawbacks: suture, autograft, allograft, or xenograft. In the last years novel solutions were proposed: scaffolds that temporarily replace the damaged part, promoting the junction regeneration, then degrading when the healing process is completed. The electrospinning technique has become increasingly popular for the manufacturing of these structures during the years, becoming one of the main processes used by researchers in this field. This technique allowed the production of porous nanofibrous scaffolds using biodegradable, but above all biocompatible, polymers. The purpose of this review thesis is to cover all the available studies in literature that employ electrospinning to produce scaffolds for interfaces, thus obtaining an overview of the progress made and the various techniques used.

Abstract

L'apparato muscolo scheletrico è composto da strutture muscolari, articolari e ossee. Tali tessuti sono molto diversi tra loro e hanno proprietà meccaniche estremamente variabili, pertanto presentano una transizione graduale in corrispondenza della loro giunzione, onde evitare l'insorgere di concentrazioni di tensione. L'evoluzione ha portato alla formazione di particolari interfacce che permettono la corretta trasmissione dei carichi distribuendo le tensioni su una superficie più ampia in corrispondenza della giunzione. Le interfacce che vanno a inserirsi nell'osso vengono definite entesi e in particolare, in questa review, analizzeremo il caso di quelle tra tendini/legamenti e osso. In questo lavoro ci siamo anche concentrati sulla giunzione miotendinea, ovvero tra muscolo e tendine. Sono numerose le lesioni che riguardano muscoli, ossa, tendini o legamenti e molto spesso l'infortunio avviene a livello della giunzione. Quando ciò accade vi sono diverse strade, ciascuna con i suoi vantaggi e svantaggi: sutura, autograft, allograft o xenograft. Oltre a queste soluzioni si è fatta gradualmente più spazio la possibilità di realizzare degli scaffold che vadano temporaneamente a sostituire la parte danneggiata e a promuovere la sua rigenerazione, degradandosi man mano. L'elettrofilatura (Elettrospinning) è un processo produttivo che negli ultimi decenni si è affermato come tecnica per la fabbricazione di questi scaffold, fino a diventare uno tra i principali processi utilizzati dai ricercatori in questo campo. Questa tecnica infatti permette di realizzare scaffold di nanofibre porose utilizzando polimeri biodegradabili e soprattutto biocompatibili. Lo scopo della review è proprio quello di scoprire tutti i lavori e gli studi che utilizzano l'elettrofilatura per realizzare degli scaffold per interfacce, delineando così lo stato dell'arte sui progressi fatti e sulle varie tecniche utilizzate.

Contents

1. Introduction

The electrospinning technique is getting increasing attention in the tissue engineering research field. Faithfully mimicking the fibrillar level of aggregation of several tissues, such as the tendinous, ligamentous, muscular and bony ones, it has demonstrated to allow the cell proliferation and the extracellular matrix (ECM) production. Parallelly to several studies focused on the regeneration of single specific tissues, mainly in the last ten years researchers have started to explore the possibility to develop dedicated strategies to regenerate multi-tissue structures. Focusing on the orthopaedic side of the problem, this review will present a comprehensive overview on the electrospinning strategies adopted to produce scaffolds suitable for the regeneration of the tendon/ligament (T/L) to bone (enthesis) and the myotendinous interfaces. This review is thought to show firstly a general overview of the different interfaces function, biology and mechanics, as well as on the basic electrospinning requirements, techniques and materials to design these scaffolds. Then, with a bottom-up approach, the different electrospinning techniques and scaffolds will be investigated and described from the cellular, *in vitro* and *in vivo* and the mechanical point of view.

1.1 Musculoskeletal system: main tissues and their interfaces

The musculoskeletal system is composed of several tissues that work together ensuring the physiological movements. The main characteristic of these different tissues is their hierarchical structures, organized in different scale levels. Focusing on the musculoskeletal structural and motor tissues, the hard-structural component of this complex kinematic chain is the bone (Weiner and Wagner, 1998). It is a hard-mineralized tissue, mainly composed at the nanoscale level of collagen type I fibrils doped with hydroxyapatite (Hap) nanocrystals (from a few hundred nanometers to 1 μm), that aggregates each other producing flat structures called lamellae (diameters = 1 - 10 μm). As a sort of building blocks of the bone tissue, the assembly of several lamellae generates several micrometric fundamental features of bones: Haversian systems, osteons and trabeculae (diameters = 10 - 500 μm) that aggregate in different percentages generating the related cortical (osteons) or cancellous (trabeculae) bone (Rho et al., 1998). Other elements that compose the bone tissue are finally blood vessels, nerves and the bone marrow

(Weiner and Traub, 1992). The cellular component of the bone tissue is constituted by the osteocytes, osteoblasts and osteoclasts that, working together, control the bone system homeostasis.

These mineralized natural joints are actuated by the skeletal muscles. Muscles are contractile tissues structured in a fibrous and hierarchical way. They are composed of water, proteins, salts, minerals, fat, and carbohydrates (Frontera and Ochala, 2015). The protein content mainly consists in collagen (Type I, III, IV and V) for the tissue membranes (i.e. endomysium, perimysium, epimysium (Light and Champion, 1984)), and myosin, actin and titin for the contractile parts (i.e. sarcomeres) (Frontera and Ochala, 2015).

The contractile element of muscles is the sarcomere, which is composed, at the nanoscale, of different protein filaments, called myofilaments. Sarcomeres are connected through a flat region called the Z-line. The myofilaments are divided in thick (myosin), thin (actin) and elastic (titin) ones. Thin and thick filaments slide on each other along the H-zone, the region without any overlaps, generating the contraction. The overlap of myofilaments produces the typical striated appearance of muscles. Sarcomeres are connected to each other both in a parallel and longitudinal ways. Thousands/millions of sarcomeres form the myofibril (diameter = 1-2 µm). Several myofibrils, parallelly arranged and wrapped inside a sheath of connective tissue called endomysium, produce the myofiber (diameter = 10-100 µm) (Frontera and Ochala, 2015). Myofibers are the structural unit of skeletal muscles, composed by a single, polynucleated cell called myocyte (Frontera and Ochala, 2015). Inside and all-around the myofibers, the sarcoplasmic reticulum is found, whose main function is to store calcium ions (Ca^{2+}), essential for contraction. Bundles of myofibers form a muscle fascicle (hundreds of microns) that is surrounded by the perimysium (Light and Champion, 1984). Then groups of fascicles, bundled together, generate the whole muscle belly. The whole muscle is covered by a layer of dense, irregular connective tissue sheath named epimysium.

Other two key-features in the musculoskeletal tissues are tendons and ligaments. Tendons and ligaments are fundamental soft tissues for the human movement since they have the task respectively of transmit the force between muscles and bones (tendons) and to guarantee the physiological joints alignment (ligaments)

(Arruda et al., 2006; Nukavarapu et al., 2015). As for the muscular tissue, also tendons and ligaments are characterized by a complex multiscale fibrous structure. They are composed of water and extracellular matrix (ECM) that is mainly constituted by collagen type I (smaller amounts also of type III, V, X, XI, XII and XIV are present), elastin and proteoglycans (Murphy et al., 2016). The basic unit of tendons and ligaments is the tropocollagen molecule (Wang, 2006). Tropocollagen molecules aggregate producing the collagen fibril (diameter = 10–500 nm), the smallest structural unit of these tissues (Wang, 2006). Bunch of collagen fibrils generate collagen fibers that aggregate to produce primary fiber bundles (called also sub-fascicles), and a group of primary fiber bundles forms a secondary fiber bundle (or fascicle) (diameters form 1 up to hundreds of microns). Finally, groups of secondary fascicles form a tertiary bundle, and groups of tertiary bundles aggregate producing the whole tendon or ligament (surrounded by the epitenon/epiligament membranes) (Kannus, 2000). The structures from fibers to tertiary fiber bundles instead are surrounded by thin collagen membranes called endotenon/endoligament, which contain blood and lymphatics vessels and nerves (Kastelic et al., 1978; Kannus, 2000; Wang, 2006).

The cellular component, composed by fibroblasts or tenocytes, is arranged in rows between the collagen fibers (Murphy et al., 2016; Santos et al., 2017). These such different tissues, in terms of compositions, functions and mechanical properties, are connected each other with dedicated and fine-tuned junctions. These junctions are fundamental to guarantee a physiological transfer of loads reducing at minimum the stress concentrations between them. Nature have answered to this issue by adopting progressive gradients of ECM organization/mineralization to shift from one tissue to another (Nukavarapu et al., 2015). These optimized interfaces are so able to effectively reduce these relevant concentrations of stress, caused by a difference of one/two orders of magnitude in terms of modulus of elasticity among the two tissues (i.e. muscle to tendon or T/L to bone interfaces), driving also the progressive phenotype changes of the cellular component. In particular, the interface between the T/L to bone tissue is called enthesis, while the connection between the tendon and muscle tissue is named myotendinous junction (MTJ) (Z. Paxton, 2013).

1.2   Entheses and myotendinous junction

1.2.1 Structure

The interface between T/L and bones, the enthesis, can widely vary depending on the particular anatomical side and tissues involved. However, two main enthesis categories are univocally recognized as main relevant: the fibrous enthesis (indirect) and the fibrocartilaginous enthesis (direct). In the fibrous enthesis, tendons and ligaments are connected through acute angles to bones with the Sharpey's fibers (8-25 µm) (Genin et al., 2009), collagen fibers that extend directly from the bones and their periosteum (for example in the tibial insertion of the medial collateral ligament) (Yang and Temenoff, 2009). The fibrocartilaginous enthesis instead (for example the femoral insertion of the medio collateral ligament) is characterized by a progressive mineralization gradient (Figure 1) described by four main zones (Yang and Temenoff, 2009): the T/L side, the unmineralized fibrocartilage, the mineralized fibrocartilage and the bone tissue. Starting from that, the T/L tissue starts a progressive loss in anisotropy of its highly aligned collagen fibrils and a consequent increase in the mineralization content. The first tissue found in this process is the unmineralized fibrocartilage which contains collagen types II, III and a small amount of collagen types X, IX and I, as well as proteoglycans (mainly aggrecans) with associated chondroitin 4- and 6-sulfate glycosaminoglycans (GAGs) (Font Tellado et al., 2015). In this zone the collagen fascicles have an increased section and the collagen fibrils have increased their randomicity, while fibroblasts and tenocytes left the space to ovoid-shaped aligned fibrochondrocytes (Yang and Temenoff, 2009). The boundary section between the unmineralized and the mineralized fibrocartilage is called tidemark (Apostolakos et al., 2014). Then the mineralized fibrocartilage is found and continues up to the bone tissue, progressively losing fiber alignment and increasing the amount of Hap. In this zone it is possible to observe hypertrophic chondrocytes surrounded by type II and X collagen and aggrecans (Nukavarapu et al., 2015). In in the fibrocartilage region the mean diameter of fibers ranges approximately between 10-20 µm (Rossetti et al., 2017). Finally, the bone tissue is found with and ECM mainly composed by collagen type I and Hap, surrounded by osteoclasts, osteocytes and osteoblasts (Baldino et al., 2015). The

enthesis tissue is estimated to be generally 500 μm thick along the T/L to bone junction (Rossetti et al., 2017).
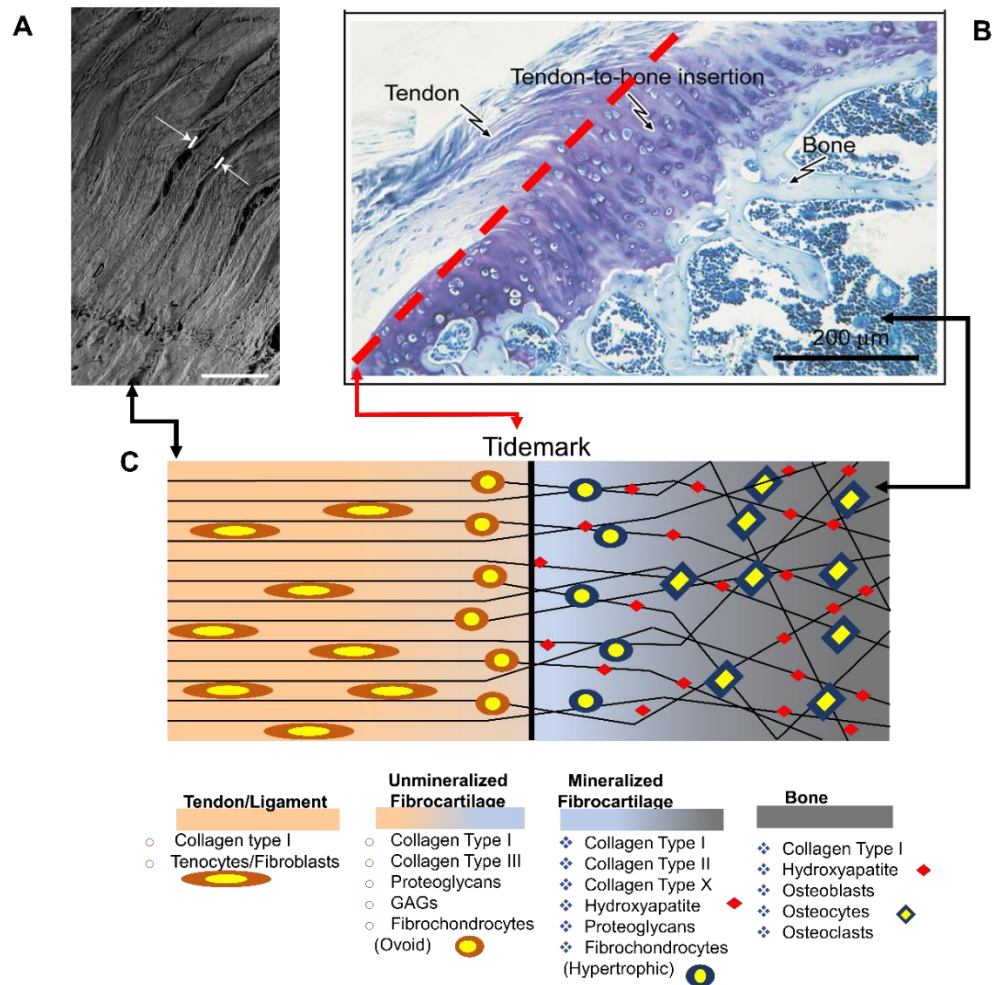

Figure 1. Tendon/Ligament to bone interface. (A) View of the tendon fibers observed with the scanning electron microscopy (SEM) (Scale bar 250 μm) adapted from (Rossetti et al., 2017). (B) Histologic section of a rat supraspinatus tendon to bone interface obtained with toluidine blue strain adapted from (Smith et al., 2012). (C) Graphical representation of the tendon to bone insertion and its components.

At the opposite side of the enthesis, the MTJ guarantees a gradual transition between the stiff tendon and the smooth muscle tissue. Conversely to the enthesis, which is constituted by a continuous gradient of mineralization and fibrous organization of the ECM, the MTJ connects each other a mainly cellular tissue (muscles) and prevalent ECM structure (tendons). At the macroscale, the MTJ creates a network of overlap between muscle and tendon tissues, enhancing their surface of adhesion (Figure 2). From a micro- and nanometric point of view instead, the myofibers at the MTJ generate conical finger-like projections

interdigitating the tendon ECM (Charvet et al., 2012). Each muscle projection is formed by an aligned network of actin filaments matched with actin-binding proteins that originate from the Z-bands, giving to the projections their conical shape and stiffness (VanDusen and Larkin, 2015). This intracellular matrix connects to subsarcolemma and intramembrane focal adhesion protein complexes, anchoring the muscle cytoskeleton to the tendon ECM. Several focal adhesion complexes are present at the MTJ, containing proteins such as talin, vinculin, and paxillin (Tidball et al., 1986; Turner, 2000). The adhesion complexes connect to the actin matrix of the sarcolemma projections, the transmembrane proteins α7 integrin and the dystrophin-associated glycoproteins, which join to the extracellular laminin, anchoring the muscle cytoskeletal proteins to the tendon ECM (VanDusen and Larkin, 2015).
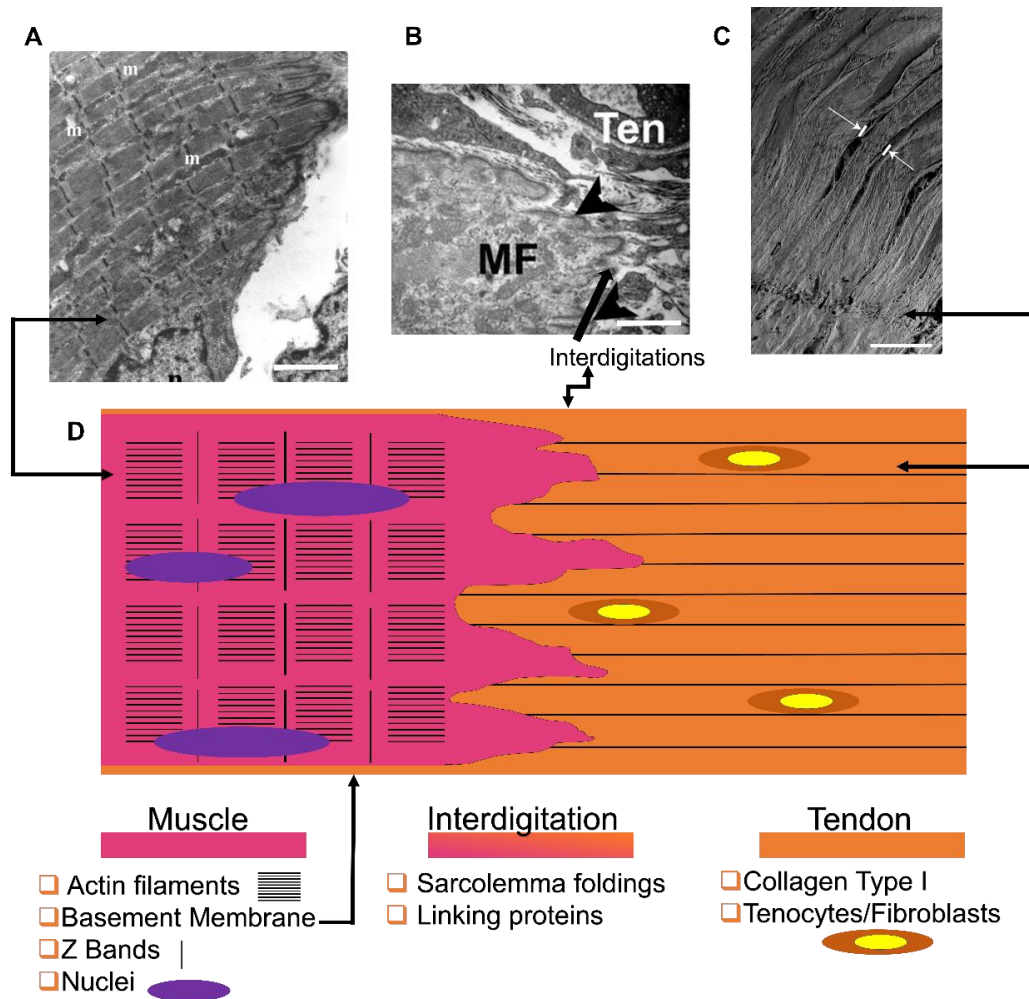
Figure 2. The myotendinous junction. (A) TEM image of the arrangement of the sarcomeres and a peripheral nucleus on the bottom (Scale bar 1 μm) adapted from (Curzi et al., 2013). (B) SEM image of finger-like processes that characterize the myotendinous junction (MF = muscle fibers; Ten = Tenocytes) (Scale bar 1 μm) adapted from (Kostrominova et al., 2009); (C) View of the tendon fibers observed with the scanning electron microscopy (SEM) (Scale bar 250 μm) adapted from (Rossetti et al., 2017) . (D) Graphical representation of the myotendinous junction and its components.

1.2.2 Mechanical properties

The main characteristic of natural tissues mechanical behaviour resides in its nonlinear mechanical properties (Fung, 1993; Murphy et al., 2016). Moreover, this non-linearity is strongly dependent on the degree of mineralization of the tissue of interest (Fung, 1993; Murphy et al., 2016). In anisotropic and not mineralized fibrous tissues, such as tendons, ligaments and muscles, a strong nonlinear behaviour of the stress-strain curves is observed, in particular in the toe-region. Here, after the application of a load, the fibrils/myofibers are progressively stretched, from their resting crimped state, up to their complete alignment occurring in the linear region (Maganaris and Narici, 2005; Gotti et al., 2020b). Because of the mineral content, in the bone this nonlinear behaviour is reduced and strongly dependent on its percentage of cortical and cancellous tissue (Rho et al., 1998). Moreover, moving from the muscle, T/L and finally to the bone tissue, the mean values of some mechanical properties (e.g. failure strain and failure stress) widely vary, some of which (e.g. Young's Modulus) sometimes more than one order of magnitude (Table 1) (Murphy et al., 2016). The bone tissue is the stiffer (both in tension and compression) with a Young's Modulus in the range of 14.0 - 21.8 GPa (cortical) (Reilly and Burstein, 1975; Morgan et al., 2018) and 0.37 - 24.7 GPa (cancellous) (Oftadeh et al., 2015; Murphy et al., 2016), a yield strain of 1.0 - 3.1% (cortical) (Murphy et al., 2016; Morgan et al., 2018) and of 0.3 - 2.8 % (cancellous) (Røhl et al., 1991; Murphy et al., 2016) and a failure stress of 82.9 - 150.6 MPa (cortical) (Reilly and Burstein, 1975; Mirzaali et al., 2016) and of 13.3 - 33.2 MPa (cancellous) (Kopperdahl and Keaveny, 1998; Murphy et al., 2016). T/L instead, show lower values of Young's Modulus (i.e. tendons: 65 - 2310 MPa; ligaments: 23 - 724 MPa) (Murphy et al., 2016) compared with the one of the bone tissues but with similar values of failure stress (i.e. tendons: 24 - 112 MPa; ligaments: 1 - 46 MPa) (Murphy et al., 2016). Concerning the failure strain instead, for tendons is in the range of 14 - 52 % and for ligaments of 8 - 120 % (Smith et al., 1996; Murphy et al., 2016). Finally the skeletal muscle has the lower mechanical properties compared with the aforementioned tissues, with a range of Young's modulus of 30 - 8000 kPa, a failure stress of 70 - 800 kPa and a failure strain of 30-60 % (Lännergren, 1971; Halpern and Moss, 1976; Moss and Halpern, 1977; Kuthe and Uddanwadiker, 2016; Schleifenbaum et al., 2016; Gotti et al., 2020a).

Considering these extensive ranges of mechanical properties, the connection between such different tissues is fundamental to reduce the possible stress concentrations and guarantee a progressive material gradient while avoiding unexpected failures in these interfaces. Considering the wide range of mechanical properties of these tissues, also those of enthesis and MTJ vary considerably between different individuals and anatomical sites. Moreover, since these interfaces are generally of limited extension, it is also particularly difficult to effectively estimate their mechanical strength without considering partial contributions from surrounding tissues.

Stating from the entheses, these interfaces have to connect the rigid and stiff bone tissue with the softer and more elastic T/L one. This is achieved through an increasing gradient of mineralization moving from the T/L to the bone tissue, while conversely decreasing y the degree of anisotropy of the fibrillar component (Font Tellado et al., 2015). However, very few works tried to investigate the mechanical properties of the enthesis in literature. In particular Deymier et al., performing a tensile test through an atomic force microscope, focalized their attention on the rat supraspinatus tendon to bone interface, finding an average failure stress of 45.7 ± 3.4 MPa, a Young's Modulus of 3.1 ± 0.9 GPa and a failure strain of 4.3 ± 3.3 % (Deymier et al., 2017). In later studies the same authors continued to investigate the supraspinatus enthesis mechanical properties, calculating a failure stress of 33 ± 35 MPa (Deymier et al., 2019) and also tested the supraspinatus rat enthesis, obtaining a Young's Modulus ranging from 20 - 80 MPa and a failure stress of 8 - 20 MPa (Deymier et al., 2020)

Conversely, the MTJ has not to guarantee a mineral gradient, but has the fundamental function to connect a very smooth and elastic tissue (skeletal muscle) to a fibrous and a one order of magnitude stiffer tissue (tendon) (VanDusen and Larkin, 2015). This purpose of stress concentrations reducer is guaranteed by its particular interdigitated surface in which the myofibers ends are covered by terminal portions of tendon fibrils that cross them mixing with the endomysium and perimysium membranes. The myotendinous junction does not show a gradient in mineralization, but there would still be a stress concentration problem because the tendon is stiffer than the muscle. Moreover the MTJ has to convey the muscular contraction to the tendon tissue, permitting the transmission of the mechanical force (Madhurapantula et al., 2017). Thanks to the interdigitation, the

MTJ is able to distribute the load over a wider area so as to reduce tensions on the interface portion, since it is a critical area. Moreover this particular structure allows to decrease the angle of loading on the interface, which places the interface primarily under shear stress (Yang and Temenoff, 2009). Even in this case very few studies tried to investigate the mechanical behaviour of the MTJ. An example of MTJ mechanical properties from pig diaphragms were shown in the Ladd et al. work (Ladd et al., 2011), in which they found an elastic modulus of 0.28 ± 0.15 MPa, a failure stress of 0.15 ± 0.02 MPa and a strain at failure of 122.4 ± 19.2 % (Ladd et al., 2011). In another work Zhao et al. investigated the mechanical properties of the distal and proximal sides of pig Achilles tendon-triceps surae MTJs, finding a Young's Moduli of 90 MPa (distal) and 70 - 150 MPa (proximal), failure stresses of 20 - 40 MPa (distal) and 40 - 60 MPa (proximal) and failure strains of 45 - 75 % (distal) and 35 - 55 % (proximal) (Zhao et al., 2018). Azizi et al. studied the mechanical behavior of the turkey gastrocnemius MTJ, finding a Young's Modulus of 744 ± 219 MPa, a failure stress of 53.2 ± 12.9 MPa and a failure strain of 8.6 ± 4.2 % (Azizi et al., 2009).

Table 1. Mechanical Properties of the tissues

Tissue	Young's Modulus	Failure Stress	Failure Strain	References
	MPa	MPa	%	
Bone				
Cortical (human)	14000 - 21800	82.9 - 150.6	1.0 - 3.1	(Reilly and Burstein, 1975; Mirzaali et al., 2016; Murphy et al., 2016; Morgan et al., 2018)
Cancellous (human)	370 - 24700	13.3 - 33.2	0.3 - 2.8	(Kopperdahl and Keaveny, 1998; Oftadeh et al., 2015; Murphy et al., 2016)
Tendon (human)	65 - 2310	24 - 112	14 - 52	(Smith et al., 1996; Murphy et al., 2016)
Ligament (human)	23 - 724	1 - 46	8 - 120	(Murphy et al., 2016)
Muscle (human)	0.03 - 8	0.07 - 0.8	30 - 60	(Lännergren, 1971; Halpern and Moss, 1976; Moss and Halpern, 1977; Kuthe and Uddanwadiker, 2016; Schleifenbaum et al., 2016; Gotti et al., 2020a)
Enthesis	3100	2-49	1-61	(Deymier et al., 2017; Li et al., 2017; Song et al., 2019; Reifenrath et al., 2020)
Supraspinatus	3.1 ± 0.9	45.7 ± 3.4	4.3 ± 3.3	(Deymier et al., 2017)

(rat)				
Supraspinatus (rat)	-	33 ± 35	-	(Deymier et al., 2019)
Supraspinatus (rat)	20 - 80	8 - 20	-	(Deymier et al., 2020)
MTJ				(Tidball, 1991; Ladd et al., 2011)
Diaphragm (pig)	0.28 ± 0.15	0.15 ± 0.02	122.4 ± 19.2	(Ladd et al., 2011)
Achilles tendon - Triceps Surae (pig)				(Zhao et al., 2018)
Distal	∼ 90	20 - 40	45 - 75	(Zhao et al., 2018)
Proximal	70 - 150	40 - 60	35 - 55	(Zhao et al., 2018)
Gastrocnemius (turkey)	744 ± 219	53.2 ± 12.9	8.6 ± 4.2	(Azizi et al., 2009)

1.2.3 Surgical approaches

Lesions regarding muscles, tendons, ligaments and bones are very common. Although the entheses dissipate the stress away from the interface, there are many cases of tear and wear (Benjamin). Often the anatomic sites of injury involve intra-articular entheses like the rotator cuff and the anterior cruciate ligament (ACL) or extra-articular entheses as the Achilles tendon and the medial collateral ligament (Derwin et al., 2018). The injuries of the enthesis often result in severe disability and may cause complications such as the osteoarthritis, that is estimated to affect over 70% of people in the range of 55 - 78 years old (Boys et al., 2017). This impacts for example on the United States finances for 213 billion dollars every year (Patel et al., 2018). Entheses lesions are a very widespread phenomenon since 20 - 80% of people between 50 - 80 years have been found to be affected by a rotator cuff tear (Yamamoto et al., 2010), which is one of the most common injuries in this field. Moreover, the failure rates after surgeries for enthesis repair are extremely high (e.g. rotator cuff: 20-94%; ACL: 10-25%) (Po-Yee Lui et al., 2010). Moreover, the younger patients are not away from risk as they could be affected by acute or overuse sport injuries like tennis elbow and jumper's knee injuries (Calejo et al., 2019). There are approximately 2 million Achilles tendon sports related injuries in the world every year. Of them, over 250000 require surgical intervention (Baldino et al., 2016). However, the enthesis could be affected by external and internal factors, which are not necessarily related with sports injuries and that could cause problems at the junction site (Calejo et al., 2019). These problems are known as enthesopathies. When an inflammation process occurs, it is also termed as enthesitis, which is a common pathological condition in sports injuries (Benjamin et al., 2002). The enthesitis is also significant for the capability to diffuse idiopathic hyperostosis (DISH), which is a degenerative condition represented by a superfluous deposition of bone at the fibrocartilage zone (Benjamin et al., 2002). Surgical procedures are often associated with high failure rates (11-95%) (Apostolakos et al., 2014).

Also the MTJ has a great risk of injuries, which are mainly caused by stress concentrations produced by unpredictable peaks of muscular contractions and strains (Speer et al., 1993). MTJ injuries are classified in 3 degrees: (i) first degree

includes small lesions that heal without adverse sequelae; (ii) second degree comprises partial tears and (iii) third degree results in complete tears (Palmer et al., 1999): In the first degree lesions, the MTJ shows limited lesions and edemas which heal without any permanent consequences (Taneja et al., 2014). In the second degree, a partially ruptured junction is showed and, depending on the damage entity, long-term functional impairing, pain and recurrent injury may occur. These injuries are treated with a conservative approach that generally restore the muscle strength and its range of motion (Palmer et al., 1999). The surgical approach to manage the third degree (i.e. total rupture) of MTJ injuries depends on several factors such as the patient's age, the rupture site and the actual range of motion.

A possible way to repair injured interfaces is provided by biological grafts (i.e. auto-, allo- and xeno-). An autograft is a portion of biological tissue from the same patient used to repair the damaged site, while an allograft/xenograft uses a decellularized tissue portion from a human or animal donor, respectively. Even if the main advantage of autografts is the low rejection rate (Vang, 2006), they suffer from high surgery times, multiple surgical sites and, most of all, they repair a lesion producing another one at a different patient's site (Vang, 2006; Boys et al., 2017). The advantages of an allograft instead, are the smaller incisions and the reduced surgery time, that is particularly relevant for those patients who could have anaesthesia-related complications (Vang, 2006). Their disadvantages instead are the high costs, the tissue sizing, the donor availability, and most of all the tissue rejection. Moreover if they are not correctly sterilized, they can transmit to the patients viral infections like HIV or hepatitis (Robertson et al., 2006; Vang, 2006; Boys et al., 2017). Xenografts have similar performances of allografts but with the additional risk of causing zoonosis to the patients if they are not correctly sterilized and decellularized (Grove, DPM, 2008).

All the limitations of biological grafts makes particularly challenging the regeneration of the enthesis and MTJ, so researchers moved their attention to the realization of synthetic scaffolds able to mimic the structure of these interfaces, trying to improve the overall outcomes of these surgical approaches. For this reason, this particular branch of tissue engineering is named "interfacial tissue engineering" (Bonnevie and Mauck, 2018).

1.3 Requirements for a scaffold for interfacial tissue engineering

In order to guarantee a biomimetic reproduction of the structure and mechanics of the target biological tissue, scaffolds have to satisfy some requirements, which are essential to achieve an effective healing:

(i)   Biocompatibility: scaffolds must be accepted by the human body and not considered as a foreign object. This means that cells have to recognise the scaffolds surface as biomimetic and adhere and proliferate on them as they are seeded onto a biological tissue. The poor biocompatibility could cause inflammatory processes, infections or a foreign body rejection (Chen et al., 2009; O'Brien, 2011).

(ii) Biodegradability: scaffolds must be engineered to have a controlled degradation over time leaving cells to replace them with new ECM (O'Brien, 2011). The degradation rate is fundamental in fact, if it is too high, cells are unable to proliferate on them (Sung et al., 2004). Moreover the degradation process must not release toxic components causing inflammations (O'Brien, 2011).

(iii) Porosity: scaffolds must be porous, allowing the cellular infiltration and proliferation (Loh and Choong, 2013), allowing also the clearence of waste products from the scaffolds themselves (O'Brien, 2011).

Moreover, in the case of the interfacial tissue engineering other specific properties are mandatory:

(iv) Mechanical properties: the mechanical properties should be congruent with the site of implantation, protecting the interfaces from peaks of load until the regenerated ECM is not strong enough to carry on by its own these mechanical stresses (Chen et al., 2009). Scaffolds must also follow the mechanical behaviour of the different tissues of the target interfaces, ensuring proper gradients of stress, strain and stiffness to speed up the cellular proliferation and the ECM production (Nukavarapu et al., 2015). A proper mechanical behavior is also fundamental to drive the stem cell differentiation in the different regions of these scaffolds.

(v)   Morphology: scaffolds must follow the morphology of the different tissues that are going to temporarily replace. This implies the production of continuous gradients of fibers orientations and structure, reproducing their progressive loss of anisotropy (i.e. from T/L to bone) or their continuous alignment with changes in materials (i.e from muscle to tendons and vice versa) (Zhang et al., 2012).

(vi)   Mineralization (for enthesis only): T/L to bone entheses present a gradation in mineral content, which starts at the tidemark and intensifies along the mineralized fibrocartilage and cancellous bone tissue. A dedicated scaffold for the regeneration of these tissues needs to show this mineral gradient (Zhang et al., 2012).

Considering all these requirements, researchers started to design and investigate several types of scaffolds and manufacturing techniques for the regeneration and replacement of both the enthesis and the MTJ with promising preliminary results (Ladd et al., 2011; Zhang et al., 2012; Font Tellado et al., 2015). However, considering the complex hierarchical fibrous structure of these interfaces and their related tissues, among the several techniques explored, the electrospinning is for sure one of the most promising (Ladd et al., 2011; Baldino et al., 2015). This technique in fact has widely demonstrated to faithfully reproduce the hierarchical fibrous structure and the biomechanical properties of the T/L, the skeletal muscles and the bone tissue, enhancing the cellular proliferation and ECM production both *in vitro* and *in vivo* (Mo et al., 2004; Ramachandran and Gouma, 2008; Jang et al., 2009; Rothrauff et al., 2017; Sensini and Cristofolini, 2018; Sensini et al., 2019; Gotti et al., 2020b, 2020a). Moreover, the electrospinning has also carried out encouraging preliminary results in the interfacial tissue engineering research field (Ladd et al., 2011; Baldino et al., 2015).

1.4   Electrospinning

Focusing on the electrospinning, it is a simple and versatile technique to produce fibers which range in diameter from a few micrometers down to the nanoscale (Bosworth and Downes, 2011). Thanks to this ability it has attracted, mainly in the last three decades, an increasing attention in several research fields (Ramakrishna et al., 2006). In fact, this micro- and nanometric fibers production

method has constituted a real ground-breaking revolution in particular in the tissue engineering field when researchers started to realize its ability to mimic the ECM of the natural tissues and to drive the cellular proliferation and growth (Ramakrishna et al., 2005; Bosworth and Downes, 2011). The physical phenomenon behind the electrospinning is really simple, and starts when a natural or synthetic polymeric viscoelastic solution, in which the target polymer (or blends of polymers) is solved in a dedicated solvent system, is extruded, at a controlled flow-rate, by a syringe with a metallic needle (Figure 3). The needle is charged with a positive voltage of several kilovolts, placed at the opposite side of a metallic collector posed at ground potential. This electrical setup generates an high electrostatic field that causes the distribution of positive charges over the surface of the polymeric solution droplet, extruded by the needle (Haider et al., 2018). The positive charges are attracted to the ground collector, causing the stretching of the polymer droplet. When the force produced by the positive charges overcome the surface tension of the droplet, it starts to assume a conical shape (called Taylor's Cone) and from the tip of this cone a fiber is finally drawn. During the flying phase from the needle to the ground collector, the repulsive forces between the charges placed on the surface of the fiber cause the whipping of the fiber itself. The whipping allows contemporary the evaporation of the solvent and reduces the diameter of the fibers that finally reach the collector surface producing a non-woven mat (Bosworth and Downes, 2011). Despite the electrospinning is theoretically a simple technique, it is influenced by several parameters which directly affect the resulting nanofibers (Haider et al., 2018). These parameters are conventionally grouped in three macro categories (Ramakrishna et al., 2005):

(i)   Solution parameters: these parameters are directly related to the polymers and solvents used to obtain the solution (i.e. molecular weight of the polymers involved, solution viscosity, surface tension, solution conductivity and dielectric constant of solvents and their boiling points).

(ii)   Process parameters: these parameters are related to the mechanical, electrical and technological setups adopted to electrospun the nanofibers (i.e. applied voltage, feed-rate, collector shape and movement, diameter and structure of the needle, movement of the needle, number of needles, needle-collector distance).

(iii)   Environmental parameters: these parameters are generally the more difficult to manage and are directly related to the electrospinning environment (i.e. relative humidity, temperature and pressure).
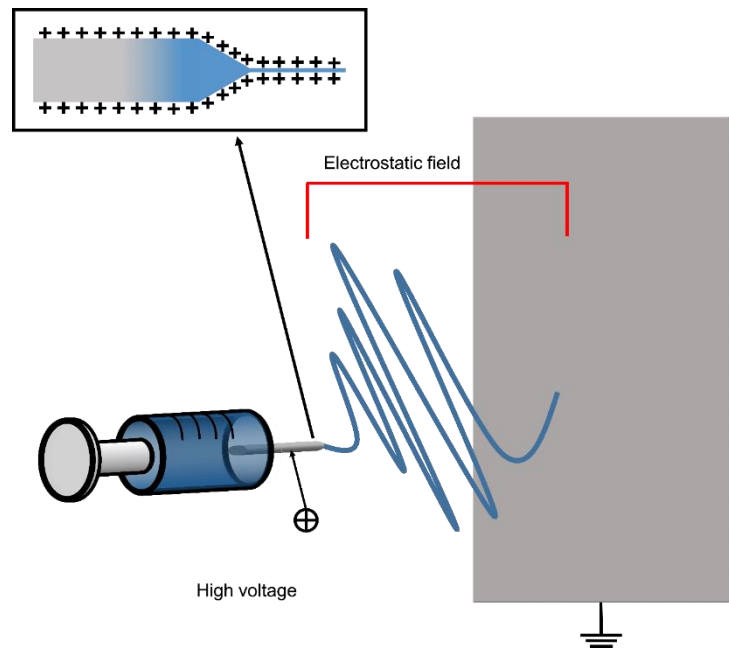

Figure 3. A basic electrospinning process setup

By the fine tuning of all these parameters it is possible to obtain several shapes, morphologies and structures of the nanofibers, modifying also their mechanical properties (Ramakrishna et al., 2005). Conversely, if these parameters don't reach an equilibrium, the resulting nanofibers will be characterized by the presence of beads on their length or eventually the electrospinning can produce just a spray of droplets (Ramakrishna et al., 2005, 2006; Haider et al., 2018). To underline the importance of some parameters mentioned above, the needle-collector distance, for example, is mandatory to obtain smooth and well-shaped nanofibers, and depends on the polymeric solution characteristics and on the applied voltage. Generally, thicker nanofibers are obtained when the distance is small and the voltage is low, whereas the nanofibers become thinner when distance and voltage are increased. Also, the solvents are fundamental to avoid the formation of beads: too volatile solvents, because of their low boiling points and high evaporation rates, can cause a premature dry of the jet at the needle tip, blocking the electrospinning process. Less volatile solvents are also to be avoided too because they can cause an incomplete evaporation during the flight, resulting in wet fibers

on the collector. Moreover, humidity affects the evaporation speed of the solvent as at low humidity the solvent dries faster compared to higher ones, compromising the quality and structure of the nanofibers. Other focal parameters for the electrospinning are also the shape and the movement of the ground collector. In particular, by modifying these two settings, it is possible to control the orientation and shape of the nanofibers produced (Figure 4-5). The most common collector is the metallic flat plate. With such morphology the nanofibers obtained have an isotropic randomly arranged orientation (Figure 4A). The same arrangement can be obtained by using a drum collector rotating with a peripheral speed < 8 m s^{-1} (Figure 4B). The random mats obtained with these two collectors configurations are for example particularly suitable to reproduce the typical structure of the cancellous bone or the fibrocartilage as well as their degrees of porosities (Jang et al., 2009; Bhattarai et al., 2018). When the peripheral speed is ≥ 8 m s^{-1} the nanofibers start progressively to be aligned along the circumference of the drum, obtaining a progressive anisotropic unidirectional orientation (Figure 4C). Another easy method to reach the same nanofibers orientation is the application of the so called "gap collector" setup (Figure 4D). The gap collector mainly consists in two metallic rods or bars, placed at ground potential, with a free space between them: the nanofibers attracted by the ground potential of the two collectors will align filling the gap previously produced. However, this method allows the alignment of the nanofibers only when a very limited gap is produced (generally less than 100 mm). Moreover, after the removal of the axially aligned nanofibrous mat from the drum or gap collectors, depending from the kind of polymer used, the collector rotational speed or the gap distance, it is possible to observe a shrinkage of the nanofibers. This property allows to confer to these uniaxial mats the typical morphology and nonlinear mechanical properties typical of the skeletal muscle and T/L tissues (Bosworth and Downes, 2011; Sensini and Cristofolini, 2018; Gotti et al., 2020a, 2020b).

Furthermore, to develop gradients of random and aligned nanofibers as well as continuous regions with different materials, several dedicated electrospinning procedures and setups were designed. Some typical examples are constituted by the multilayer electrospinning or the co-electrospinning (Figure 4E and F). The multilayer electrospinning consists in the production of a first mat of nanofibers (random or aligned) and a further electrospinning of an additional mat, with the

same or a different polymeric solution, on the previous one (again both aligned or randomly arranged) (Figure 4E). The co-electrospinning instead consists in the simultaneous electrospinning of two different solutions on a drum or flat collector in order to obtain mats with two different types of nanofibers (Figure 4F). Both these two electrospinning configurations resulted particularly suitable to mimic the tissue and fiber-orientation gradients of the enthesis and the MTJ (Ladd et al., 2011; Xie et al., 2012; He et al., 2017). Moreover some groups have tried to modify these setups in order to obtain defined regions with completely different materials suitable for example to mimic the ligament to bone interface (Figure 5A) (Samavedi et al., 2014). In this case scaffold with a central aligned region and two continuous random sides were obtained by electrospinning different solutions on two drums rotating at low speed (< 8 m/s) (random nanofibers = bony sides), connected by a central rod. The central gap between the drums was suitable to produced aligned nanofibers, resembling the ligament tissue arrangement (Samavedi et al., 2014). Generally, the electrospinning technique produces mats of nanofibers but, changing the collection device and properly adjusting the electric field, it is possible to obtain organized filaments of nanofibers called bundles or twisted ones named yarns (Abbasipour and Khajavi, 2013). Thanks to this, nanofibers have been employed in a wide area of applications; in particular, bundles have an extremely important role in the reproduction of the hierarchical structure of the tendons and ligaments (O'Connor and McGuinness, 2016; Sensini et al., 2019). So far, we have discussed electrospinning as a technique, finding it a very promising method. Therefore, some researchers have started to think about the combination of electrospinning with other additive manufacturing (AM) procedures to better reproduce the structure of biological tissues and to realize scaffolds never seen before (Figure 5B). Additive manufacturing techniques cannot produce fibers in the nanometric range, while electrospinning has some limitations in reproducing 3D structures; hence these techniques compensate each other (Dalton et al., 2013). A pioneering study was conducted by Criscenti et al., who firstly realized a 3D printed structure and then used it as a target for the electrospinning process, so a triphasic scaffold was obtained (Criscenti et al., 2016).
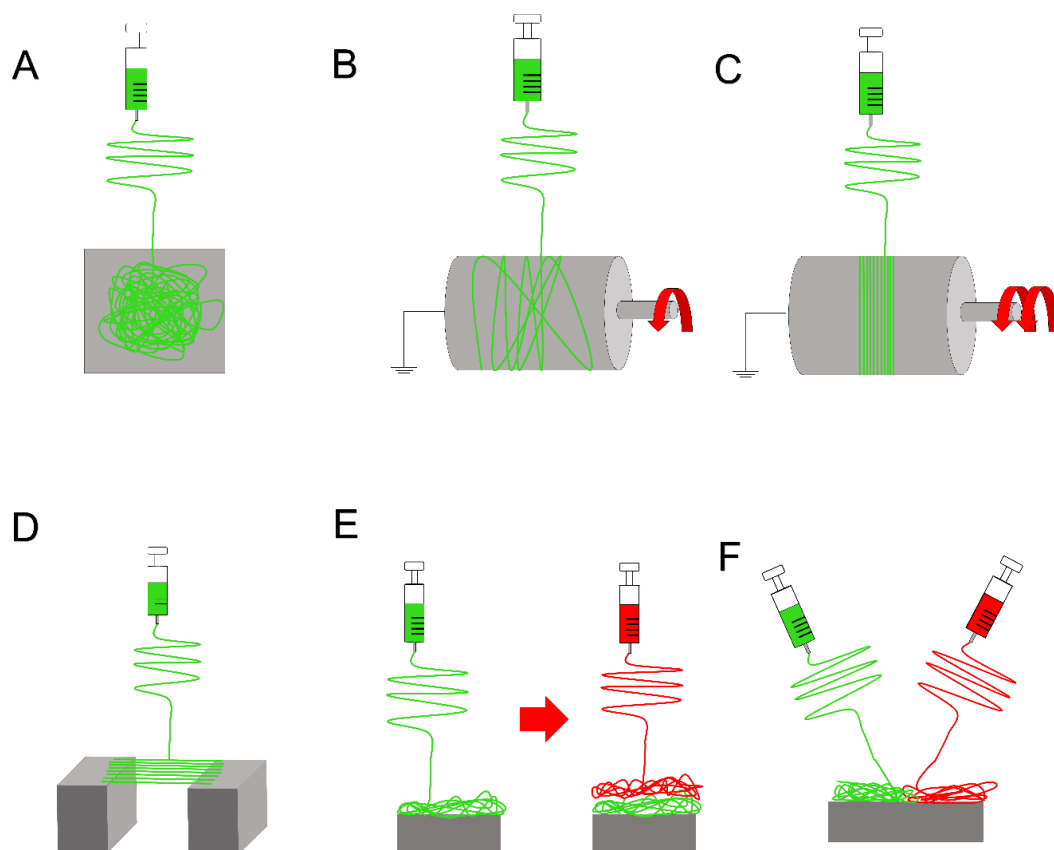
Figure 4: Electrospinning setups to produce nanofibrous mats: (A) aluminum plate (random nanofibers), (B) rotating drum at a speed < 8 m/s (random nanofibers), (C) rotating drum at a speed > 8 m/s (aligned nanofibers), (D) gap collector (aligned nanofibers), (E) multilayering electrospinning setup; first solution is spun on a flat plate collector producing a random mat, then it is used as target for the electrospinning of the second solution; (F) Co-electrospinning of two different solution on a flat plate.
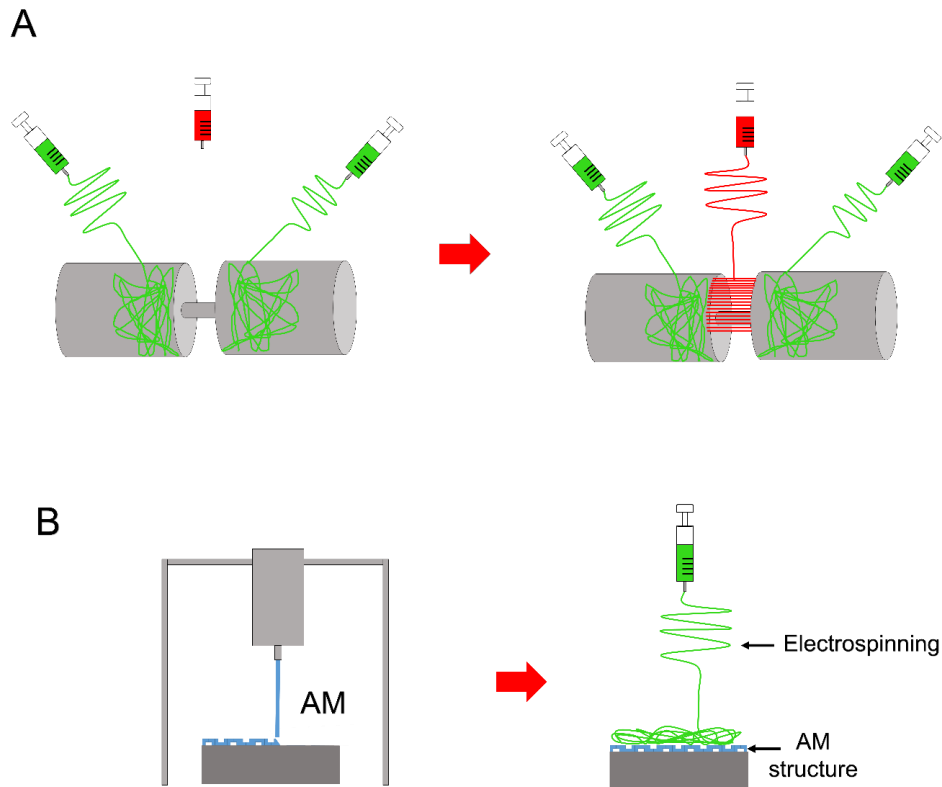
Figure 5: Electrospinning setups used to realize 3D or composite structures: (G) setup composed of two drums with a gap in between to obtain the ligament-bone mimicking structure (random-aligned-random); (H) setup for combining electrospinning and additive manufacturing, which could be a 3D printed structure to mimic the bone structure.

The materials used in the various electrospinning processes are several; among all, PLGA and PCL have found wider use, but some groups have gone further using materials such as silk fibroin. Other researchers have used blends of materials, such as the PLLA/Collagen blend. Regarding the use of the nanoparticles, nanohydroxyapatite, as well as growth factors, found a widespread employment. The following tables recap all the materials employed in the papers reported in this review: table 2 shows bulk materials, table 3 shows Blends & Core/Shells, and table 4 displays drugs and nanoparticles.

Table 2. Bulk materials

Acronym	Extended Name	Applications	References
PLGA	Poly(lactic-co-glycolic acid)	Tendon-to-Bone Interface Ligament-to-Bone Interface	(Li et al., 2009; Xie et al., 2010; Liu et al., 2011; Kolluru et al., 2013; Lipner et al., 2014, 2015; Zhao et al., 2014; Su et al., 2019) (Samavedi et al., 2014; Criscenti et al., 2016; He et al., 2017; Jiang et al., 2020)
PLGA	Poly(l-lactide-co-glycolic acid)	Tendon-to-Bone	(He et al., 2014)
PLGA	Poly(D,L-lactide-co-glycolic acid)	Tendon -to-Bone	(Spalazzi et al., 2008; Inui et al., 2012; Chou et al., 2016)
PLLA	Poly(L-lactic acid)	Tendon-to-Bone Interface Tendon-to-Muscle Interface	(Zhao et al., 2015; Baudequin et al., 2017; Li et al., 2017; Perikamana et al., 2018) (Ladd et al., 2011)
PCL	poly(ε-caprolactone)	Tendon-to-Bone Interface Ligament-to-Bone Interface	(Li et al., 2009; Xie et al., 2012; Han et al., 2015, 2019; Bayrak et al., 2016; Baudequin et al., 2017; Nowlin et al., 2018; Wu et al., 2018; Zhu et al., 2019; Lin et al., 2019; Song et al., 2019; Reifenrath et al., 2020) (Samavedi et al., 2011, 2012, 2014; Criscenti et al., 2016; Lin et al., 2017; Olvera et al., 2017)
SF	Silk Fibroin	Tendon-to-Bone Interface	(Zhi et al., 2016; Cai et al., 2018)
PD	Polydopamine	Tendon-to-Bone Interface	(Perikamana et al., 2018; Lin et al., 2019)
PEUU	Poly(ester urethane urea)	Tendon-to-Bone Interface	(Huang et al., 2019)
PUR	Polyurethane	Ligament-to-Bone Interface	(Samavedi et al., 2012)
BPUR	Biodegradable poly(ether ester urethane urea)	Tendon-to-Bone Interface	(Kishan et al., 2017)
PEUUR2000	Poly(ester urethane urea) elastomer	Ligament-to-Bone Interface	(Samavedi et al., 2011)
Gelatin	Gelatin	Tendon-to-Bone Interface	(Li et al., 2009; Zhao et al., 2015)
CS	Chitosan	Tendon-to-Bone Interface	(Wu et al., 2018; Han et al., 2019; Reifenrath et al., 2020)
HA	Hyaluronic acid	Tendon-to-bone Interface	(Han et al., 2019)
Col	Collagen	Tendon-to-Bone Interface	(Han et al., 2015; Chou et al., 2016; Lin et al., 2019)

Table 3. Blend & Core Shell

Acronym	Type	Applications	References
SF/P(LLA-CL)	Blend	Tendon-to-Bone Interface	(Cai et al., 2018)
PCL/CS	Blend	Tendon-to-Bone Interface	(Wu et al., 2018)
PCL/Col	Blend	Tendon-to-Bone Interface Tendon-To-Muscle Interface	(Han et al., 2015; Lin et al., 2019) (Ladd et al., 2011)
PCL/PLLA	Core Shell	Tendon-to-Bone Interface	(Baudequin et al., 2017)
CS/HA	Blend	Tendon-to-Bone Interface	(Han et al., 2019)
PLGA/Col	Blend	Tendon-to-Bone Interface	(Chou et al., 2016)
Li+@MSNs/PEUU	Blend	Tendon-to-Bone Interface	(Huang et al., 2019)
PLLA/Col	Blend	Tendon-to-Muscle Interface	(Ladd et al., 2011)

Table 4. Drugs and particles

Acronym	Extended Name	Applications	References
bFGF	Basic Fibroblast Growth Factor	Tendon-to-Bone Interface	(Zhao et al., 2014)
nHap	Hydroxyapatite	Tendon-to-Bone Interface Ligament-to-Bone Interface	(Liu et al., 2011; Kolluru et al., 2013; He et al., 2014; Han et al., 2015; Bayrak et al., 2016; Li et al., 2017; Wu et al., 2018) (Samavedi et al., 2011, 2012; He et al., 2017; Jiang et al., 2020)
PDGF-BB	Platelet Derived Growth Factor-BB	Tendon-to-Bone Interface	(Perikamana et al., 2018)
SDF-1α	Stromal cell-derived factor 1	Tendon-to-Bone Interface	(Han et al., 2019)
BMP-2	Bone morphogenetic protein 2	Tendon-to-Bone Interface Ligament-to-Bone Interface	(Lipner et al., 2015; Han et al., 2019) (He et al., 2017; Jiang et al., 2020)
Melatonin	Melatonin	Tendon-to-Bone Interface	(Song et al., 2019)
GO	Graphene Oxide	Tendon-to-Bone Interface	(Su et al., 2019)
KGN	Kartogenin	Tendon-to-Bone Interface	(Zhu et al., 2019)
Li+	Lithium	Tendon-to-Bone Interface	(Huang et al., 2019)
TGF-β3	Transforming growth factor beta-3	Tendon-to-Bone Interface Ligament-to-Bone Interface	(Reifenrath et al., 2020) (Jiang et al., 2020)

2. Aim of thesis

This work aims to provide an overview of the current state of the art regarding the studies that employ the electrospinning to realize scaffolds for interfacial tissue regeneration. The thesis also provides a showcase of the main outcomes in particular for the cellular and mechanical tests. Moreover, since recently a technology able to faithfully reproduce a human tendon was developed at the University of Bologna, there is a remarked interest to also reproduce the insertion sites, with particular attention on the tendon to bone enthesis. This thesis therefore aims to represent a starting point and a guide for future experiments in the field of regeneration of musculoskeletal interfaces.

3. Search strategy

A methodical search using PubMed, Science Direct and Google Scholar databases was carried out in order to find papers relevant to the electrospinning technique for the T/L to bone and muscle to tendon enthesis. With this aim, the search terms used were "electrospinning" combined with ''tendon-bone,'' "tendon-bone healing," "ligament-bone," "ligament-bone healing/repair," "muscle-tendon junction," "myotendinous junction", "enthesis". For the introduction part, the research strategy made use of the following terms: "tendon structure", "ligament structure", "Bone structure", "muscle structure", "electrospinning", "enthesis", "tendon-bone interface", "ligament-bone interface", "muscle-tendon interface", "myotendinous junction", "tendon-bone injuries", "myotendinous junction injuries", "enthesis mechanical properties", "myotendinous junction mechanical properties", "scaffolds for interface regeneration"
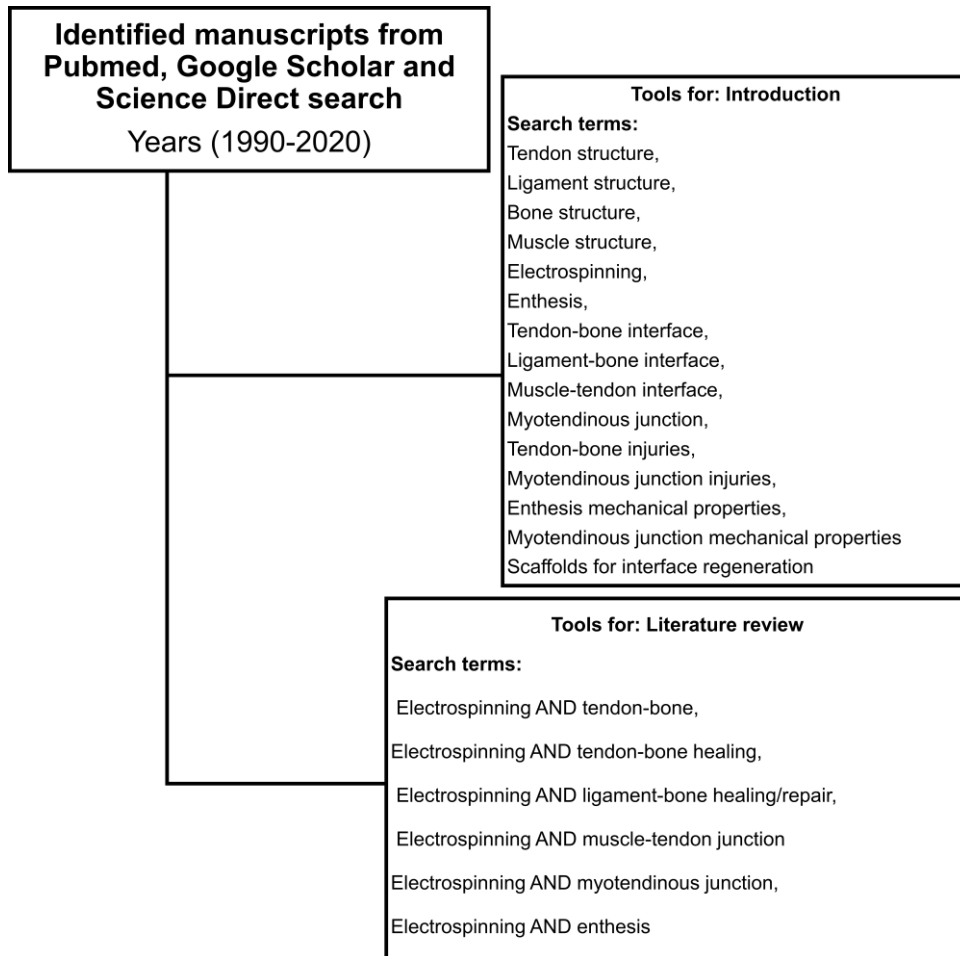
Figure 6: Search strategy for the introduction and results of the literature review part.

4. Results of the literature review

In this section we made an accurate analysis of the research articles by classifying them according to a hierarchical complexity of the realized scaffolds:

1. Simple mats
2. Biphasic mats
3. Multilayer mats
4. Composites e 3D structures

At the end of this part there 3 tables, which display information about the results of the mechanical or biomechanical tests (Table 5), the *in vitro* cell culture (Table 6) and the *in vivo* experiments (Table 7).

Simple Mats

By Applying a bottom-up approach, some groups started to mimic the fibrous arrangement of tissue interfaces, by electrospinning simplified 2D nanofibrous mats. In particular Li et al. in a very preliminary study, aiming to regenerate the tendon-bone junction, fabricated random nanofibrous mats coated with a continuous gradation of calcium phosphate (Li et al., 2009). The scaffolds were realized by electrospinning PCL or PLGA random nanofibers on an aluminum foil. After their production, the resulting membranes were plasma treated and then mineralized with a ten-times simulated body fluid (10SBF) for 2 to 6 hours (Figure 7), creating a mineral gradient. The mechanical tests were carried out using a digital image correlation approach and evaluated only on stripes of PLGA mats where investigated. After the application of 3 different stress values (0.3 MPa, 1.4 MPa and 2.2 MPa), the PLGA specimens showed that the values of strain increased with the decrease in the mineral content (0.3 MPa: from ~ 0% up to ~ 2% of strain; 1.4 MPa: from ~ 1% up to ~ 4% of strain; 2.2 MPa: from ~ 0% up to ~ 7% of strain), while the modulus of elasticity decreased with the decrease in the mineral content (from ~ 120 MPa in the mineralized side, to ~ 30MPa in the unmineralized one). For the *in vitro* culture, only the PCL random mats with the mineral gradient were seeded with mouse calvaria-derived preosteoblastic cells (MC3T3- E1; ATCC CRL-2593). Before the cultures, the PCL mats were also covered with gelatin. The cellular proliferation analysis showed, after 3 days of culture, a more intense cell density on the mineralized end compared with the

unmineralized one, where very few cells were observed (Li et al., 2009). With the same purpose Liu et al. applied a new method to mineralize an electrospun mat of PLGA (Liu et al., 2011). Firstly they produced aligned nanofiber mats by electrospinning a PLGA solution on a rotating mandrel, then before the mineralization procedure, they were firstly bathed in a watery solution of chitosan, EDC-NHS and 2-(N-morpholino)ethane sulfonic acid (MES), and then in a 1% heparin Dimethylaminopropyl)-N′-ethylcarbodiimide hydrochloride (EDC)- N-Hydroxysuccinimide (NHS)-MES one. Subsequently the mats were immersed into a modified 10 times concentrated simulated body fluid (m10SBF), for different time intervals (i.e. 0, 2 and 6 hours), to cover them with Hap. The authors tested the mechanical properties of mats, subjected to different times of mineralization, showing that the modulus of elasticity increased with the mineral content (0 hours = 250 MPa; 2 hour = 350 MPa; 6 hours = 560 MPa) while no statistically differences were observed for the yield stress (0 hours = 7 MPa; 2 hour = 6 MPa; 6 hours = 7.5 MPa). This new method of mineralization surely resulted in a denser and thicker coating than the previous works, even if the mechanical properties resulted lower compared to the bone tissue (Liu et al., 2011). In another study, Inui et al. evaluated the effects of the enthesis healing in a infraspinatus rabbit model (Inui et al., 2012). They fabricated random mats of PLGA nanofibers that were implanted in 42 rabbits. After 16 week the histological tests revealed an expression of collagen type I, II and III at the tendon side and a new cartilage formation at the enthesis side. The biomechanical tests, which were carried out on an infraspinatus tendon-scaffold-humeral head complex, showed that there were no statistically differences between the group treated with the scaffolds and the control one concerning the stiffness (scaffold group = 8.25 ± 2.17 N/mm; control group = 7.725 ± 1.85 N/mm) and load to failure (scaffold group = 45.075 ± 11.3 N; control group = 54.075 ± 13 N) (Inui et al., 2012). Kolluru et al. studied the mechanical behavior of as spun, mineralized and unmineralized, nanofibers designed for the healing of tendon-bone enthesis. The PLGA nanofibers were collected on metallic frames placed close to a flat aluminum collector. The unmineralized nanofibers were treated with a plasma cleaner, obtaining 3 different shapes: i) uniform circular cross-section with sparse surface irregularities; ii) uniform ellipsoidal cross-section and iii) non-uniform/rough cross-section along the entire nanofiber length. The mineralized

ones instead, were obtained by soaking the nanofibers at different time points (from 5 to 30 min) in 10SBF, obtaining 3 increasing thickness of mineralized Hap coatings, called respectively: i) thick-platelet mineral coating on top of an inner conformal layer of mineral; ii) thick-conformal mineral coating, and iii) thin-conformal mineral coating. The micromechanical tests, carried out on the single fibers, showed that the tensile strength was higher for the unmineralized groups (unmineralized = 96.6 ± 7.3 MPa; mineralized = 77.6 ± 15 MPa) as well as the yield stress (unmineralized = 53.3 ± 4.6 MPa; mineralized = 37.6 ± 6.6 MPa) compared to the mineralized ones, while no statistical difference was found in elastic moduli (unmineralized = 1.76 ± 0.16 GPa; mineralized = 1.77 ± 0.19 GPa) (Kolluru et al., 2013). Zhao et al. concentrated their studies on the rotator cuff tear (RCT). They realized random PLLA membranes grafted with gelatin (Zhao et al., 2015). Firstly, they prepared the membrane by electrospinning, then they lyophilized and sterilized them before the gelatin modification, which was achieved with an amynolysis method previously developed. Cell proliferation was evaluated up to 7 days culture with mouse fibroblasts (C3H10T1/2). The membrane effect on the RCT healing was also evaluated *in vivo* on 144 rats, which were randomized in 3 groups (control group, PLLA group and gelatin-PLLA group) and sacrificed at different time points. The cell proliferation assay showed a higher proliferation on the gelatin-PLLA compared to the pure PLLA group. The histological analysis evinced that on the gelatin-PLLA membranes, after 8 weeks of implantation, a greater GAG staining area as well as their ability to boost new cartilage formation was noted. The biomechanical tests confirmed the promising outcomes of the gelatin-PLLA mats after 8 weeks of trials: a greater failure load (32 N), stiffness (15 N/mm) and failure stress (1.75 MPa) compared to the other groups (PLLA group: failure load = 28 N, stiffness = 13.5 N/mm, failure stress = 1.6 MPa; control group: failure load = 26 N, stiffness = 13 N/mm, failure stress = 1.65 MPa) (Zhao et al., 2015). In another study Zhao et al., with the same aim of promoting the RCT healing, fabricated a random electrospun membrane, loading the nanofibers with a basic fibroblast growth factor (bFGF) (Zhao et al., 2014). The scaffold was produced by electrospinning a solution of PLGA and bFGF. *In vitro* cell culture was carried out with human dermal fibroblasts (HDFs), while an *in vivo* study was made on 144 rats, which were divided into 3 groups (control group, PLGA group and bFGF-PLGA group) and sacrificed at

different time points for the histomorphometric and the biomechanical analysis. After 5 days of culture, the *in vitro* test revealed a higher cellular proliferation in the bFGF-PLGA membranes compared to the pure PLGA ones. After 8 weeks of implantation, the histological analysis reported the formation of fibrocartilaginous tissue and a significantly greater area of glycosaminoglycan (GAG) as well as an improved collagen organization for the bFGF-PLGA than the other groups. The biomechanical tests pointed out the increase of mechanical properties with time and a particularly higher failure load and stiffness in bFGF-PLGA compared to the other groups after 8 weeks of implantation (failure load: control group = 27.1±1.2 N, PLGA group = 28.4 ± 1.2 N, bFGF–PLGA group = 32.7 ± 1.0 N; stiffness: control group = 13.0 ± 0.7 N/mm, PLGA group = 13.7 ± 0.7 N/mm, bFGF–PLGA group = 14.9 ± 0.3 N/mm). Moreover, at the same time point, a greater failure stress was found in the bFGF-PLGA (bFGF–PLGA = 1.82 ± 0.03 MPa) compared to the other groups (control = 1.65 ± 0.09 MPa, PLGA = 1.62 ± 0.03 MPa). This work introduced for the first time in the field the possibility of loading drugs or particles in the electrospinning solutions trying to increase the cellular differentiation power of nanofibers (Zhao et al., 2014).The mechanical behavior was the center of Lipner et al. studies who focused on aligned PLGA electrospun scaffolds with a gradation in mineral content for the tendon-bone insertion site (Lipner et al., 2014). The PLGA scaffolds were fabricated, cut into smaller pieces and finally plasma treated (to increase their hydrophilicity). Subsequently two different groups were produced: a first one was treated with a mineralization consisting in a modified 10SBF protocol, and then incubated 4 hours with heparin and for additional 4 hours with chitosan and the EDC crosslinker; the second one instead was simply mineralized with a 10SBF protocol. The membranes were then soaked in a 10SBF solution for 30 min and subsequently in another 10SBF one (normal or modified) to apply the mineralization. Mineralization with simple 10SBF appeared plate-like and diffuse while m10SBF mineralization was dense and conformal to the fibers (Lipner et al., 2014). The mechanical tests revealed that the higher strain was observed on the lower mineralized region and that the denser mineral coating produced on the m10SBF samples resulted in a more rapid stiffening compared to 10SBF group (Lipner et al., 2014). In another work Lipner et al. deepened their previous study by investigating the impact of the same aligned PLGA mats, seeding them with

adipose derived stem cells (ADSCs) before the implantation (Lipner et al., 2015). After the electrospinning process the mats were plasma treated and then mineralized with 10SBF thus becoming ready for being implanted on 64 rats. One group of scaffolds was realized by loading the nanofibers with nanoparticles bone morphogenic protein 2 (BMP2). The scaffolds were then divided in four groups: control, acellular, cellular and cellular-BMP2. The histologic analysis revealed, after 8 weeks of implantation, a delayed healing response for all the scaffold groups compared to suture-only control group. Moreover mechanical properties, after 8 weeks of *in vivo* test, were significantly decreased for the scaffolds groups (acellular: failure load = 31.1 ± 9.4 N, stiffness = 25.9 ± 10 MPa, failure strain = 34 ± 7 %; cellular: failure load = 31.7 ± 10 N, stiffness = 25.6 ± 9.4 MPa, failure strain = 38 ± 11 %; cellular-BMP2: failure load = 32.6 ± 6.6 N, stiffness = 24.4 ± 8.3 MPa, failure strain = 50 ± 20 %) compared to the control (failure load = 32.3 ± 4.9 N, stiffness = 31.9 ± 7.5 MPa, failure strain = 31 ± 8 %). In general, the scaffolds showed lower biological and mechanical performances on the enthesis regeneration compared to the control group. In particular the mechanical properties resulted even more decreased in the cellular-BMP2 group suggesting that this growth factor is not a good candidate for the enthesis healing (Lipner et al., 2015). Han et al. produced a random PCL/nHAP/Col membrane to promote tendon-bone healing (Han et al., 2015). The blend solution was electrospun on an aluminum foil plate, then the collected mat of nanofiber was cut in circular specimens and seeded with MC3T3-E1 murine preosteoblasts cells. The scaffolds were employed for an *in vivo* study on 24 rabbits, which were divided into 2 groups (PCL/nHAP/Col group and PCL group) and sacrificed after 4 and 8 weeks post-surgery. The histological analysis demonstrated a higher proliferation rate for PCL/nHAP/Col membrane and new bone formation after 8 weeks. Moreover, the mechanical properties observed in the PCL/nHAP/Col group (failure load = 58.4 ± 4.1 N; stiffness = 15.2 ± 1.4 N/mm) were higher than the PCL group ones (failure load = 39.9 ± 3.4 N; stiffness = 10.2 ± 1.3 N/mm). This study combined, for the first time, three synthetic and natural biomaterials for the tendon-bone healing: the PCL as bulk material; the nHap to speed up the bone regeneration; and the Col to enhance the T/L healing.(Han et al., 2015). Bayrak et al. used a multiple spinneret electrospinning to report the fabrication of meshes to promote tendon-bone repair (Bayrak et al., 2016) . A solution of PCL and a second

suspension of nHap were loaded into opposite syringes and co-electrospun on a rotating drum collector, obtaining random mats of PCL nanofibers with nHap particles in between on. The highest concentration of nHap observed was 16.02± 0.41%. Fiber diameters and pore size were analyzed showing an increased fiber diameter for nHap loaded nanofibers, but no significant differences on the mean pore size and their distribution. As expected contact angle was smaller in nHap loaded nanofibers because of the hydrophillicity of nHap (Bayrak et al., 2016). In another study, Zhi et al. tested the influence of electrospun random mats of silk fibroin (SF) to enhance the tendon-bone healing in a rabbit model (Zhi et al., 2016). After the electrospinning process the resulting SF mats were cut in rectangular specimens, which were seeded with bone marrow derived mesenchymal stem cells (BMSCs). The *in vitro* test indicated a better proliferation on nanofibrous membranes than on the coverslips. The *in vivo* study was made on 32 rabbits, sacrificed at 6 or 12 weeks postoperatively. In the control group, Achilles tendon was just transplanted, while in the experimental group the Achilles tendon was wrapped with SF mat before transplantation. The histological analysis revealed new bone formation in the SF mat group and a complete absorption of the mat at 6 weeks. Mechanical properties increased with time and, after 12 weeks, were found higher, in terms of failure load, in the SF mat group (~75 N) compared to the control one (~50 N) (Zhi et al., 2016). Kishan et al. produced gradient meshes of biodegradable polyester urethane urea (BPUR) at different weight ratios (BPUR50-50% wt and BPUR10-10% wt) (Kishan et al., 2017). The solution of BPUR10 had a decreasing flow rate from 0.3 to 0 ml/hr (-0.06 ml/hr) while the BPUR50 solution had an increasing flow rate from 0 to 0.3 ml/hr (+ 0.06 ml/hr), so the first fibers were mainly composed of solution 1 while the last fibers were primarily composed of solution 2 (Kishan et al., 2017). To fabricate random gradient mats an aluminum wheel was used and was rotated 90° over 6 hours, whereas to realize aligned gradient ones, a wheel with 8 parallel coper wires served as collector. Cell cultures were carried out with bone marrow derived human mesenchymal stem cells (hMSCs), which were seeded on the specimens for 3 days showing that cells were aligned with the fiber orientation on the aligned meshes while no particular orientation was observed in the random ones. The mechanical tests showed that BPUR10 had the lowest modulus (~1.8 MPa for Random Gradient and ~2 MPa for Aligned) and the highest failure strain

((~210 % for Random Gradient and ~190 % for Aligned), while an opposite behavior was observed in BPUR50 region (modulus = ~12.3 MPa for Random Gradient and ~17 MPa for Aligned; failure strain = ~145 % for Random Gradient and ~75 % for Aligned). Compared to the studies, this one introduced the concept of materials gradient, which is an important point for a scaffold for interface regeneration. (Kishan et al., 2017). Chou et al. combined a biodegradable collagen-loaded random membrane and a 3D printed anchoring bolt to promote tendon-bone repair. The nanofibrous mat was produced by electrospinning a blend of PLGA/Col at different (v/v) ratios (40/60 v/v, 50/50 v/v, 67/33 v/v, 80/20 v/v, 100/0 v/v). The *in vitro* cell cultures results exhibited higher proliferation rates of the human fibroblasts for mats with a high collagen ratio, due to the increased hydrophilic behavior. The 67/33 v/v mesh had the highest proliferation rate and, because of this, it was chosen for the *in vivo* testing. The random mesh system was transplanted with the long digital extensor tendon in half of 48 rabbits used for the *in vivo* evaluation, while the remaining 24 rabbits were used as control. The rabbits were sacrificed 8 and 16 weeks postoperative. Histological analysis showed new bone formation and biomechanical tests revealed higher values of the mean failure load for the bolt-mesh group (41.4 N) compared to the control (28.3 N) after 16 weeks (Chou et al., 2016). Baudequin et al. focused on cell differentiation analyzing the ability of different PCL and PLLA (pure or core-shell) mats to induce cells differentiation (Baudequin et al., 2017). With this aim, PCL and PLLA were firstly separately electrospun to obtain aligned and random mats with different nanofibers diameters and morphologies: Random PCL (diameters 600 nm and 1000 nm), aligned PCL, random PLLA, and also random core-shell mats of PCL/PLLA (PCL out-PLLA in, PLLA out-PCL in). The mechanical tests were made under dry and wet conditions. In dry conditions core-shell scaffolds scored the highest elastic moduli, in particular PCLout membranes resulted in 60.14 ± 18.52 MPa. C3H10T1/2 were used for *in vitro* test. The cellular proliferation on PCL scaffold was the most continuous and dense. Bone (Dlx5, Runx2, Bglap) and tendon (Scx, Tnmd, Aqp1) related markers expression was also analyzed. PCL membranes had the highest values of Bglap expression and the lowest values of Scx. Core-shell mats instead showed the ability to particularly influence the tenogenic differentiation with a significant Tnmd value. PLLA scaffolds were not found to be a good way to induce tendon or bone

differentiation (Baudequin et al., 2017). Olvera et al. examined the effect of growth factor stimulation on mesenchymal stem cells with the aim of improve the ligament-bone healing (Olvera et al., 2017). The cells were seeded on random and aligned microfibrillar mats of PCL, which were produced by electrospinning onto a rotating drum collector. The scaffolds were individually or sequentially stimulated with transforming growth factor (TGF-β3) and connective tissue growth factor (CTGF) by maintaining them in culture medium, ligamentum medium or a chondrogenic one. The ligamentum medium contained CTGF while the chondrogenic one contained TGF-β3. Ligamentous (Col1a1, Col3a1, acta2 and Tnmd) and chondrogenic (Col2a1, Col10a1, aggrecan and SRY-Box 9) markers expression were also evaluated. The scaffolds stimulated with TGF-β3 showed a particularly higher collagen type II expression on the aligned fibers compared to randomly oriented ones, whereas bone morphogenic protein (BMP-2) and collagen type I expression was higher in randomly oriented nanofiber scaffolds. A ligamentous differentiation was observed on CTGF stimulated aligned scaffolds with a higher expression of Tnmd (Olvera et al., 2017). Wu et al. realized a nanofibrous mesh for T/L to bone interface and explored their biological properties. Random nanofiber mats were fabricated by electrospinning a blend of PCL/CS solution loaded with nHap on a rotating drum collector (pure PCL/CS scaffolds were also produced as comparison). The nHap loaded scaffolds showed greater adhesion and proliferation of human osteoblasts (HOS) after 2 days of culture and had higher mechanical properties than pure PCL/CS ones (250.1 N for nHap-PCL/CS: mean failure load = 250.1 N; pure PCL/CS = 195 N). Furthermore, the tensile modulus of nHap loaded mesh was ~215.5 MPa, which was similar to that of the ligament tissue (Wu et al., 2018). Huang et al. directed their study in enhancing tendon-bone healing and preventing fat infiltrations by developing a random nanofibrous membrane (Huang et al., 2019). They wanted to investigate the aspect of fat infiltrations, which was not very much considered in the previous studies. The mesh was realized by electrospinning of a blend solution of PEUU and a solution of mesoporous silica nanoparticles eventually doped with lithium (Li+ @ MSNs). PEUU and Li+ /PEUU scaffolds were produced to compare them with Li+@MSNs/PEUU group. MC3T3-E1 (MC3T3-E1 Subclone 14 cells (Subclone 14 of mouse parietal anterior osteocytes) cells were seeded and cultured on scaffolds for 1, 3 and 5 days. The cytocompatibility assay evinced a

significantly difference between PEUU mat groups and control group and very few dead cells were observed after 5 days. This was confirmed in the Li+ concentration analysis, where it was found that low concentrations of Li+ could enhance the proliferation, the osteogenic differentiation and also inhibit the adipogenic differentiation whereas high concentration of Li+ inhibited the proliferation of cells. An *in vivo* study was also carried out with 144 rats. They were divided in four groups (suture only, PEUU mat, Li+/PEUU mat, Li+@MSN/PEUU mat) and euthanized 2, 4 and 8 weeks after surgery. The mechanical tests on scaffolds showed that the Li+@MSN/PEUU group had the highest modulus of elasticity (~17 MPa) but also the lower tensile strength and strain at failure (~12 MPa and 65%). The histological investigation proved the decreased fatty infiltration in Li+ mats, particularly in Li+@MSN/PEUU group at 8 weeks as well as collagen organization, which was more agreeable in Li+ groups and especially in Li+@MSN/PEUU one. In addition the biomechanical properties, which increased with time, evinced higher values for Li+ groups and notably Li+@MSN/PEUU scored the highest values of mean load to failure, stiffness and failure stress (23 N, 15 N/mm and 5.8 MPa) (Huang et al., 2019). Lin et al. produced different random nanofibrous membranes and evaluated the *in vitro* behavior when combined with tendon stem/progenitor cells (TSPCs) to boost tendon-bone healing (Lin et al., 2019). The membranes were divided according to the materials used for their fabrication: PCL, PCL/Col-I, PDA coated PCL, PDA coated PCL/Col-1. The PCL/Col-1 membranes were obtained electrospun a blend of PCL and Col-I at different volume ratios (4:1 v/v, 2:1 v/v, 1:1 v/v, 1:2 v/v), while the coating was achieved by immersing the electrospun nanofibers in PDA. Here there is something new compared to the previous works: the PDA coating, which showed to promote the osteoblasts adhesion and proliferation on biodegradable polymers. The cytocompatibility assay revealed that PCL/Col-I membranes (2:1) had the highest proliferation rate at days 5 and 7. The expression of osteogenic genes was evaluated after 4, 7 and 14 days of culture and it came out that PCL/Col-I (2:1) showed the highest expression of Col1a1 at all time points, while it was showed a significant increase of the OCN expression at 14 days. The Runx-2 expression was significantly higher in PCL/Col-I (4:1) and PCL/Col-I (2:1) group. The PDA coated specimens did not promote further osteogenic marker expression compared to the pure PCL membrane (Lin et al.,

2019). Song et al. fabricated a melatonin loaded-PCL membrane for tendon-bone repair (Song et al., 2019). The aligned nanofibrous membranes were electrospun from a PCL solution mixed with a melatonin one on a rotating drum. Pure PCL meshes were fabricated as a control group. *In vivo* studies were done on 93 rats and 90 of which were divided into 3 groups (control, PCL, melatonin-PCL group) and sacrificed at 2, 4 and 8 weeks post-surgery. The biological tests proved the cytocompatibility of PCL membranes and a good melatonin release with a percentage of 77%. A larger and enhanced collagen II area and a remarkable gene overexpression of aggrecan and SOX-9 were observed in the melatonin-PCL membranes, proving that the melatonin release stimulated the chondrogenic differentiation. Moreover, a new cartilage formation and a larger GAG area were observed particularly in the melatonin-PCL group starting from 4 weeks. Biomechanical tests showed increasing properties with time and that melatonin-PCL scored the highest properties of failure load, stiffness and failure stress after 8 weeks (melatonin-PCL: ~32 N, ~16 N/mm, ~3.3 MPa; PCL: ~27 N, ~14 N/mm, ~2.8 MPa; control: ~21 N, ~12 N/mm, ~2.2 MPa) (Song et al., 2019). Zhu et al. studied the influence on tendon-bone healing of a KGN-loaded PCL aligned nanofiber meshes electrospun on a drum collector (Zhu et al., 2019). A group 135 rats were used for the *in vivo* evaluation and divided in 3 categories (repair only, PCL membrane, KGN-PCL membrane). KGN release analysis displayed a rate of 80% release by day 20. Biological tests carried out with rat bone marrow stromal cells (rBMSCs), showed an increasing proliferation with time on all the PCL membranes from day 1 to 7. Chondrogenic and tenogenic differentiation was evaluated disclosing that the increasing amount of KGN could upregulate chondrogenic differentiation, with an optimal concentration of 100 μM. On the other hand, no tenogenic differentiation improvement was observed in KGN-PCL groups compared to the pure PCL membranes. In the histological assay new fibrocartilage was detected, which was more similar to normal native tendon in KGN-PCL group. Moreover, GAG investigation revealed that KGN-PCL had the highest GAG area at all time points. Biomechanical tests proved that PCL can improve mechanical properties, in particular KGN-PCL had the highest failure load after 8 weeks (KGN-PCL 29.7 ± 1.6 N; pure PCL 25.5 ± 0.27 N; control group 15.3 ± 0.7 N) (Zhu et al., 2019). Su et al. tried to improve further the regeneration of normal enthesis, which was not totally achieved yet, even if

considerable progress was done so far. They fabricated a GO-doped PLGA random nanofiber mat to promote tendon-bone enthesis repair (Su et al., 2019). Random mats of PLGA/GO and pure PLGA were electrospun on an aluminum flat collector. The tensile tests on scaffold revealed that tensile strength of PLGA was 2.37 ± 0.31 MPa while PLGA/GO was 2.05 ± 0.29 MPa. The *in vitro* tests showed an increased rate of proliferation of rabbit bone marrow mesenchymal stem cells (BMSCs) in the PLGA/GO compared to PLGA membranes and a similar trend was observed for osteogenic differentiation, where more distinct mineralized nodules on the PLGA/GO membrane were observed. The scaffolds performances were tested *in vivo* on 108 rabbits, which were divided into 3 groups (control, PLGA, PLGA/GO) and sacrificed at 4, 8 and 12 weeks. Histomorphometric analysis displayed a larger new cartilage formation area in the PLGA/GO than the PLGA only one as well as a greater collagen production. The biomechanical properties of the supraspinatus tendon-humerus complex increased with time and were significantly higher in the experimental groups than the control group: at 12 weeks PLGA/GO scored a failure load of ~155 N, a failure stress of ~7.9 MPa and a stiffness of ~13 N/mm; PLGA had a failure load of ~135 N, failure stress of ~6.5 MPa and a stiffness of ~12 N/mm while the control group obtained a failure load of ~120 N, failure stress of ~6.3 MPa and a stiffness of ~10 N/mm (Su et al., 2019). In another study, Reinferath et al. reported the effect of a chitosan coated PCL membrane when loaded with TGF-β3, compared to unloaded ones (Reifenrath et al., 2020). PCL aligned mats were fabricated by electrospinning on a rotating drum collector. These scaffolds were modified with chitosan grafted PCL (CS-graft-PCL), which was bounded to PCL using a self-induced crystallization method. Finally modified meshes were loaded with TGF-β3. An *in vivo* study was carried out on 17 rats, which were sacrificed 8 weeks after tendon repair surgery. Biomechanical tests revealed that the TGF-β3 loaded membranes had higher failure loads (23.2 ± 9.4 N) of CS-g-PCL (15.7 ± 9.4 N) ones, but were slightly lower than native control group values (29.6 ± 7.9 N) (Reifenrath et al., 2020). Olvera et al. continued their studies on the ligament to bone interface realizing an electrospun microfibrous scaffold functionalized with extracellular matrix (ECM) components (Olvera et al., 2020). The electrospinning setup was formed by a PCL loaded syringe pump and a grounded drum rotating at high speed so that aligned fibers were collected. After the electrospinning process

the meshes were wrapped into bundles and dismounted from the collector. Mechanical tests on scaffolds displayed a Young's modulus of 121.5 ± 3.8 MPa, a yield stress of 6.3 ± 0.09 MPa and yield strain of ∼10%. Collagen type I (Col-I), cartilage ECM (C-ECM) and ligament ECM (C-ECM) were immobilized on the scaffold by physical adsorption or covalent conjugation. As a control group no immobilized scaffolds (bare) were produced. Scaffolds were seeded with bone marrow derived mesenchymal stem cells and analyzed at day 0 and 10 for gene expression, while for cell viability they were analyzed after 1 day of cell culture. Moreover, part of the scaffold (C-ECM region) was coated with a biomimetic apatite by soaking that region in a 10 SBF solution. After 1 day of cell culture cells displayed different forms according to the region in which they were seeded. The cells on the L-ECM region had an elongated form, the ones on the C-ECM region showed a more rounded shape while the cells seeded on the collagen type I region had a mix of elongated and rounded form. The physical incorporation of every kind of protein (L-ECM or C-ECM or Col-I) promoted the COL1A1 and COL3A1 expression in MSCs. In particular L-ECM physical incorporation promoted also the expression of the specific ligamentous marker tenomodulin (TNMD) and showed better ligamentogenesis influence than the Col-I functionalization because of the higher values of COL1A1, COL3A1 and TNMD. From the opposing point of view the covalent immobilization of C-ECM resulted in the highest SOX9 expression level, which is fundamental for the cartilage formation. The differentiation was further investigated in the presence of growing factors. The scaffolds were kept in the culture media augmented with CTGF or TGF-β3. The addition of CTGF increased the expression of COL1A1, COL3A1 and TNMD in the physical immobilized L-ECM membrane and in the Col-I scaffolds. Physical immobilized L-ECM still seemed to be the best environment enhancing ligamentogenesis and chemically immobilized C-ECM still had the higher values of SOX9 expression level. TGF-β3 influence was also investigated. Higher levels of cartilage specific genes like COMP, SOX9 and ACAN were observed, but no further enhancement was found on chondrogenesis with C-ECM immobilization and TGF-β3 stimulation further. After assessing the influence of L-ECM and C-ECM on singular scaffolds an aligned triphasic scaffold was engineered. The scaffold had three different regions: immobilized L-ECM region, C-ECM region and C-ECM + Hap region. The immobilization was achieved

incubating the scaffolds in different ECM solutions with the chemical immobilization method. Cell morphology followed the trends of the singular scaffolds previously tested, showing an elongated cell body on the L-ECM region and a more rounded shape on the C-ECM and C-ECM + Hap regions. Regarding the cell differentiation, carried out after 10 days of culture, L-ECM and C-ECM regions exhibited the highest values of TNMD. The mineralized region of C-ECM + Hap displayed the highest levels of COMP, ACAN, OPN and COL10A1 expression (Olvera et al., 2020).
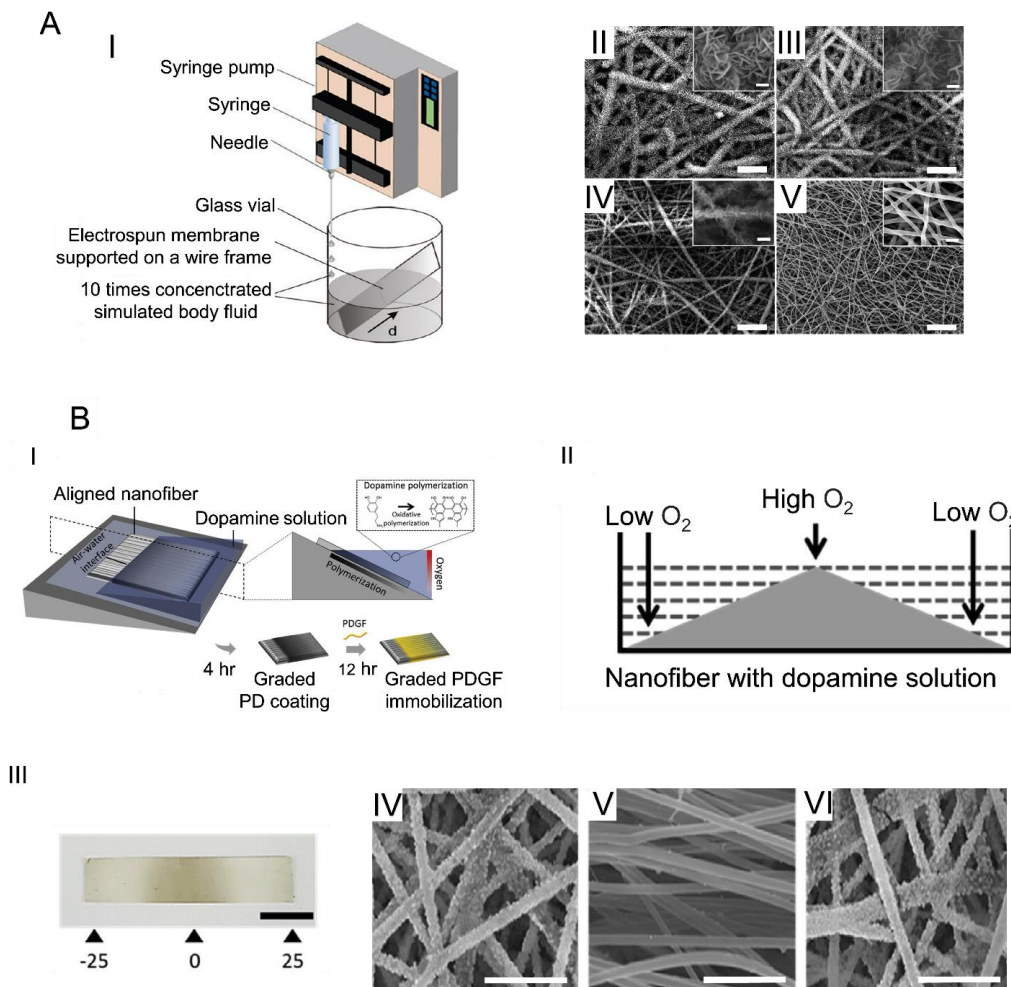
Figure 7 Procedures to produce graded mats. (A) The setup and SEM images adapted from the Li et al work (Li et al., 2009): (I) The setup used (the parameter d stands for the distance from the bottom edge of the substrate; (II-V) SEM images taken at different d values from 0 (II), 6 (III), 9 (IV) , and 11 mm (V) (scale bar = 20 μm , in the insets scale bar = 2 μm). (B) Setup used to create a gradient of PD and fabrication of a mimicking bone-patellar tendon-bone structure adapted from the Perikamana et al work (Perikamana et al., 2018): (I) Setup for a gradient in PD by controlling oxygen distribution and availability; (II) Set up for symmetrical PD gradient generation on PLLA

nanofiber surface; (III) Photograph of the symmetrical gradient obtained; (IV-VI) SEM images of the graft displaying mineralization at the ends and no minerals in the centre.

Biphasic Mats

Other research groups focused on more complex structures, trying to recreate the structural and the chemical composition of the enthesis. Indeed, they aimed to obtain aligned and random membranes to mimic the T/L, their interface and the bone tissue arrangement of the extracellular matrix. This biofabrication aspect is fundamental also to magnify the anisotropic behavior of the tissue junctions mechanical properties. With the aim of improve the tendon-bone enthesis repair, Xie et al. proposed a biofabrication strategy to electrospun an aligned to random scaffold to structurally mimic this insertion site (Xie et al., 2010). The scaffold was realized by electrospinning of PLGA on a gap collector made of two stapler-shaped metal bars to achieve the aligned (on the gap) to random (on the metal bars) structure. The biological tests performed with rat tendon fibroblasts revealed that cells on the aligned portion were axially aligned with the fibers while the cells on the random portion had a randomic pattern. Moreover collagen type I, which was preferentially unidirectional on the aligned part and random on randomly oriented side, was predominant as opposed to collagen type II. This study was an important step in the realization of scaffolds for the enthesis regeneration, developing regions with a continuous gradient of different nanofibers orientations as in the natural tissues.(Xie et al., 2010). A new electrospinning strategy was reported in the He et al. work, where a scaffold with both structure and materials gradients was realized (He et al., 2014). Their aim was to reproduce the tendon-bone enthesis by achieving a random to aligned structure and a gradation in mineralization. The setup developed for this study is showed in Figure 8. It was based on the movement of two syringes above a rotating drum, which were alternately turned on. The first syringe contained pure PLGA, while the second one was loaded with nHap-PLGA. The drum rotated at different speed to obtain random and aligned structures. The mesh was cut along the gradient direction and analyzed via X-Ray diffraction showing a continuous gradation in fiber organization but also in materials composition. He et al. clearly improved the concept introduced by Xie et al.(Xie et al., 2010) with a new electrospinning setup that allowed to obtain gradients in structure and materials, which is fundamental

for the interfacial tissue engineering (He et al., 2014). Nowlin et al. realized a random to aligned nanofibrous mat to recreate tendon-bone enthesis and promote its regeneration (Nowlin et al., 2018). The PCL mesh were electrospun on 2 parallel aluminum bars to obtain random (on the bar surface) and aligned (in the gap between the bars) nanofibers. The resulting scaffold was seeded with osteosarcomas cells and fibroblasts on random and aligned part respectively with specific cell trackers (CM-DIL for fibroblasts and CMAC for osteosarcomas). After 4 days of cellular growth fibroblasts were growing aligned with the fiber direction while osteosarcomas were not found to have any orientation. Moreover, cell migration was observed forward the mixed region since it was not seeded and a mix of both fibroblasts and osteosarcomas was displayed (Nowlin et al., 2018). Perikamana et al. produced a PLLA nanofiber mesh for tendon-bone repair. The mat was fabricated with electrospinning of a PLLA solution on a metal collector rotating at different rates to obtain random and aligned fibers. The nanofibers were then coated with dopamine and finally, platelet derived growth factor BB (PDGF-BB) was immobilized by soaking the mesh in a PDGF-BB solution. Human adipose derived stem cells (hADSCs) were seeded on the resulting scaffolds. The bioactivity was evaluated after 3 days of culture; the DNA assay was carried out at days 1, 3, 5, 7; and the Rho/Rock aspect was analyzed after 7 days. PDGF immobilized groups had a higher proliferation rate compared to the non PDGF immobilized group. In particular PDA (PDGF immobilized, polydopamine-coated, aligned PLLA nanofibers) group had the highest value of scleraxis expression, an early tenogenic factor (Perikamana et al., 2018). Samavedi et al. worked on gradations in mineral content and in composition to promote the ligament-bone regeneration (Samavedi et al., 2011). The random meshes were obtained by electrospinning on a drum collector, single mats of a PCL solution loaded with nanoparticles of Hap (nHap-PCL), a solution of PEUUR2000 and finally a co-electrospun mat of nHap-PCL and PEUUR2000. These scaffolds were cut into small pieces and covered with 5 times concentrated simulated body fluid (5SBF) for 2h to mineralize them. The mechanical characterization showed a significant increase for nHap-PCL samples in the elastic modulus compared with the not mineralized ones (0.64 ± 0.04 MPa for unmineralized and of 2.4 ± 0.23 MPa after the mineralization). PEUUR2000 samples revealed a higher failure stress than nHap-PCL ones (0.64 MPa for

mineralized and unmineralized PEUUR2000 while 0.5 MPa and 0.4 MPa after the mineralization for nHap-PCL). Cell metabolic activity was evaluated with MC3T3-E1 osteoprogenitor cells revealing that PEUUR2000 scored the highest absorbance in both cases, but it was particularly high in the unmineralized samples (Samavedi et al., 2011). Samavedi et al. tried out the response of bone marrow stromal cells (BMSCs) and their impact on the ligament-bone interface healing with a graded membrane [30]. The scaffolds were fabricated by co-electrospinning of a nHap loaded PCL solution and a PUR one on a rotating drum. The resulting scaffolds were cut into smaller pieces and divided into 3 regions (n-Hap-PCL, GRAD, PUR). The samples were treated with 5SBF to mineralize them. *In vitro* tests carried out with rat BMSCs revealed a higher metabolic activity in PUR samples and in particular in the unmineralized ones at both 1 and 7 days of culture. Osteogenic marker expression like BMP-2 and osteopontin (OPN) was higher in mineralized samples, whereas ALP expression was found to be higher in unmineralized ones (Samavedi et al., 2012). Samavedi et al. deepened their previous study designing a mesh with regions, which were differing for structure and composition to enhance ligament-bone healing (Samavedi et al., 2014) (Figure 8). These scaffolds were realized electrospinning PCL and PLGA at different (weight/weight) ratios: PCL (7.5%) – PLGA (13%) and PCL (10.5%) - PLGA (13%). A dual drum composed of two drums connected by a metal rod served as collector. Firstly, PCL was electrospun in the gap between the drums obtaining aligned nanofibers, then PCL syringe was turned off and PLGA spinning was started onto one drum. Mechanical tests showed that PLGA random fibers had a significantly higher tensile modulus than aligned PCL fibers (PLGA = 27.8 ± 7.9 MPa; PCL = 6.8 ± 3.7 MPa in PCL 7.5 -PLGA 13 and PLGA = 23.8 ± 4.4 MPa; PCL = 9.9 ± 2.6 MPa in PCL 10.5 – PLGA 13). An opposite trend was observed for failure stress which was approximately 2 times higher in PCL regions than PLGA ones. Cell morphology assay, made using BMSCs, showed no particular organization on random fibers while an alignment with fiber orientation was observed in the aligned region. Moreover, cells in the random region were polygonal, whereas cells on the aligned regions had an elongated shape. The setup adopted in this work was very innovative allowing to reproduce directly on the drum collector regions with aligned nanofibers (tendon side) and random ones (bony side). Moreover, they also used different materials to better mimic the two

tissues mechanics (Samavedi et al., 2014). He et al. also moved their attention to ligament-bone enthesis realizing a microfiber reinforced mat (He et al., 2017). The mat was realized with the same setup of the previous work (Fig. 2) to obtain random and aligned structure; moreover, the syringes were loaded with PLGA or nHap-BMP2-PLGA. Firstly, a layer of PLGA was spun on the drum obtaining aligned nanofibers, then the syringe was stopped and PLLA microfibers were wrapped around the mandrel. A new layer of pure aligned PLGA nanofibers were deposited until the microfibers were fully covered, then PLGA syringe was stopped and nHap-BMP2-PLGA one was turned on to obtain random nanofibers. The resulting meshes were seeded with MC3T3-E1, which were cultured for 2-6 days to evaluate cell morphology and proliferation, while in order to investigate the differentiation cells were cultured for 10 days. The results showed aligned cytoskeleton only in the aligned region and a high proliferation at 6 days. The differentiation assay evinced that nHap-BMP2 had much more effect on the osteogenic differentiation than structure gradient. The nanofiber mesh was further rolled to form a 3D gradient scaffold, which was mechanically tested and implanted on 10 rabbits to make a histological characterization of the scaffold. Mechanical tests were carried out with a rolled membrane of 2 or 5 cm width and they showed that Yield Force and Breaking Force significantly improved with the increasing of the width (Yield force 2 cm width = 80.25 ± 2.88 N, Yield force 5 cm width = 247.37 ± 15.63 N, Breaking force 2 cm width = 197.08 ± 9.95 N, Breaking force 5 cm width = 500.11 ± 54.17 N). After 3 months of implantation the histological evaluation revealed new collagen fibers, which were aligned with the direction of microfibers. The quantity of this newly formed fibers decreased with the gradient of nHap-BMP2. Moreover a revascularization was observed with a higher amount of blood vessels at the region with higher concentration of nHap-BMP2, while a few blood vessels were found in the region with lower nHap-BMP2 concentration (He et al., 2017). Jiang et al. wanted to investigate the differentiation capability of rat BMSCs (rat bone marrow stem cells) on nanofibrous scaffold (Jiang et al., 2020). In this work PLGA mats with a gradient of nHap-BMP2 were produced. The electrospinning setup was the same of He et al. study (He et al., 2017). After the electrospinning process TGF-β3 was uniformly added to the aligned nanofibers. After 1,4,7 days of cell culture cell morphology and viability was evaluated while differentiation was investigated

after 7 days. The viability assay showed that despite the structural and material gradients the cells had a uniform distribution. The morphology investigation evinced a disorganized cytoskeleton on the random region since the first day after seeding. This difference became more obvious at 4 and 7 days. Regarding the differentiation study, Alkaline Phosphatase Level (ALP) was found to be promoted by nHap-BMP2 in the random fiber region. Moreover, higher levels of OCN were observed on the random region as well as Runx2 expression. An opposite trend was found for Sox9 expression level, which was higher on the aligned nanofibers region. These different tendencies clearly show that structural and composition al gradient can influence the differentiation of cells (Jiang et al., 2020). Obviously not every tissue junction has a mineralizing gradient. The myotendinous junction repair does not need any mineralization gradient to be achieved since there is not the bony component. A preliminary study was made by Ladd et al. who used electrospinning to produce a scaffold in order to improve muscle-tendon junction repair (Ladd et al., 2011). The random nanofibrous membrane was obtained with a co-electrospinning technique of PLLA/Col solution and a PCL/Col solution, which were spun simultaneously on a cylindrical mandrel so as to obtain 3 regions (PCL side, PLLA side, overlap region). Mechanical tests showed that the scaffold scored 7.3 ± 2.1 MPa in tensile modulus, 0.5 ± 0.2 MPa in failure stress and 18.549 ± 8.2 % in strain at failure the native MTJ scored a tensile modulus of 0.2789 ± 0.1509 MPa, a failure stress of 0.1478 ± 0.01631 MPa and a strain at failure of $122.4 \pm 19.18\%$. PCL side underwent a greater strain then the other regions and failure occurred at that region. Biological tests carried out with C2C12 mouse myoblasts (C2C12) or NIH3T3 mouse fibroblasts revealed the formation of myotubes which was crucial for the myotendinous junction repair. The scaffold seemed also to be able to accommodate fibroblasts (Ladd et al., 2011)
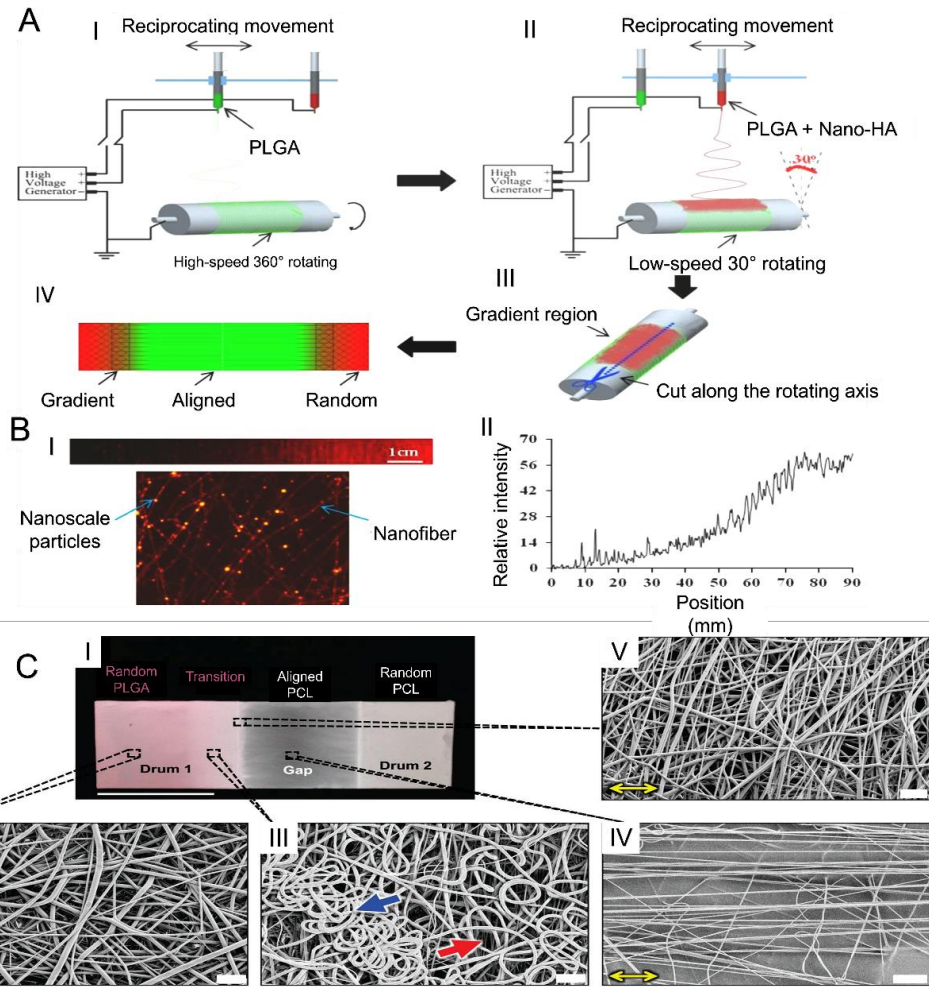
Figure 8. An electrospinning setup for biphasic mats and some SEM images. (A) Setup for electrospinning adapted from the He et al. Study (He et al., 2014): (I) Electrospinning of pure PLGA at high rotating speed to achieve the fiber alignment; (II) Electrospinning of nHap-PLGA at low speed to obtain random fibers; (III) The resulting mesh was cut along the axis; (IV) The final mat with the different regions. (B) (I) fluorescent gradient of nanoparticles; (II) fluorescent intensity of the gradient adapted from He et al. research (He et al., 2014) (C) (I) The electrospun mesh realized adapted from the Samavedi et al work (Samavedi et al., 2014); (II-V) SEM images of the mesh: (II) random PLGA region; (III) transition region; (IV) aligned PCL region; (V) edge of the transition region. (II-V) scale bar = 10 μm.

Multilayer mats

With the aim to engineering the tendon or ligament to bone enthesis researchers started also to investigate the possibility of realizing multilayer membranes that could mimic this particular junction. In particular, the multilayer configuration is useful to mimic a volumetric gradient of nanofiber organizations and materials allowing a wide surface for the cellular interaction. In a preliminary study Xie et al. produced a scaffold with structural gradients to mimic the tendon-bone insertion site. They produced the scaffolds by electrospinning of aligned PCL nanofibers on an aluminum gap collector, then the aligned mat was transferred to a glass side and served as a collector for the electrospinning of random PCL fibers. The resulting scaffolds were seeded with (ADSCs) and analyzed after 3 and 7 days of culture for cell morphology, showing that there were any cell organization on random region while cells seeded on aligned region seemed aligned along the fibers. It was a preliminary study for multilayer mats but it was an innovative approach in which the enthesis-like gradient of nanofibers alignment was reproduced along the thickness of the mat (Xie et al., 2012). In another study Li et al. explored gradients of mineralization in their scaffolds, producing a dual layer random mat to improve the tendon-bone repair (Li et al., 2017) (Figure 9). The scaffold was prepared electrospinning nanofibers of PLLA and nHap-PLLA on a rotating aluminum drum collector. Firstly, they electrospun a layer of PLLA, on which a second layer of PLLA-nHap was spun to obtain the dual layer structure. The electrospun membranes were cut into smaller pieces, which were immersed in a SBF solution for 4 days to achieve mineralization. An *in vivo* study was made on 144 rabbits which were divided into 3 groups (control, PLLA simple fibrous membrane SFM and bipolar fibrous membrane BFM). The histological analysis revealed a greater GAG staining area in the scaffold groups compared with the control and the ability of BFM to improve cartilage regeneration as well as an improved collagen organization at 12 weeks. New bone formation and higher tendon maturing score (TMS) were observed in experimental groups, in particularly BFM scored the highest TMS at 12 weeks. The biomechanical tests displayed increasing properties with time. At 12 weeks the failure load was significantly higher in BFM group than in the other ones (BFM: 181.5 ± 19.0 N; SFM: 142.7 ± 16.6 N; control: 117.1 ± 12.4 N). A similar trend was observed with the failure stress values, which were found greater in

BFM group at 12 weeks (BFM: 4.6 ± 0.6 MPa [BFM]; SFM: 3.7 ± 0.7 MPa; control: 3.5 ± 0.4 MPa) (Li et al., 2017). This work successfully explored the potential of mineralization gradients in multilayered electrospun scaffolds. In another study Cai et al. investigated the effect of an aligned-random (ARM) mat SF/P(LLA-CL) for the tendon-bone healing (Figure 9). They firstly fabricated the random part, then the aligned part was obtained on the random one with a high-speed rotating drum. Random nanofibers mats were also prepared (RM). The resulting scaffolds were crosslinked with alcohol to remove the residual solvent. An *in vivo* trial was carried out with 90 rabbits which were divided in control group (unwrapped tendon transplantation) and experimental groups (tendon wrapped with RM or ARM) and sacrificed 6 and 12 weeks post-surgery. The histological assay showed oriented collagen type I fibers and a larger area of GAG in the ARM group, while new bone formation was revealed in both scaffolds groups. Collagen type I expression was higher in the ARM group while collagen type III was significantly higher in the RM and in the control one. The biomechanical tests revealed that properties increased with time, but they were higher for the experimental groups at all time points. In particular at 12 weeks failure load and stiffness were found to value 83.2 ± 12.4 N and ~22 N/mm for ARM , 66 ± 6.6 N and ~16 N/mm for RM and 50.6 ± 3.5 N and ~10 N/mm for control group (Cai et al., 2018). Han et al. had targeted the improving of tendon-bone healing after a surgical autograft procedure by designing a layer by layer random nanofibrous scaffold (Han et al., 2019). The random PCL membrane was electrospun on a drum collector. The scaffold was coated with a CS/HA film, which was loaded with stromal cell-derived factor 1-α (SDF-1α) and BMP-2 as showed in Figure 9. The coating was achieved by a Layer by Layer self-assembly method, based on soaking firstly the PCL membrane in SDF-1α and HA solution and then in a CS and a recombinant human BMP-2 (rhBMP-2) one. This membrane was denoted as S+B@P. BMP-2 loaded PCL random mats (B@P) were also fabricated to compare them with S+B@P. *In vitro* cell culture was carried out with rat BMSCs. The cell viability and proliferation showed a higher viability and migration for the S+B@P group. Similar trends were found for the osteogenic differentiation analysis with a higher gene expression of Runx2, Osteocalcin, Col-I, OPN. 48 rabbits were used for the *in vivo* study, which were divided into 3 groups (PCL, B@P and S+B@P) and sacrificed at 4 and 8 weeks

postoperative. In the biomechanical tests S+@P group scored improved mechanical properties then B@P and PCL group, like the failure load that was 87.1% higher of that of PCL group and 25.8% higher than B@P one after 12 weeks (S+B@P: 79.9 N; B@P: 63.5 N; PCL: 42.7 N). Similar behavior was observed in the stiffness at the same time point (S+B@P: 19.5 N/mm; B@P: 13.9 N/mm; PCL: 10.8 N/mm) (Han et al., 2019).
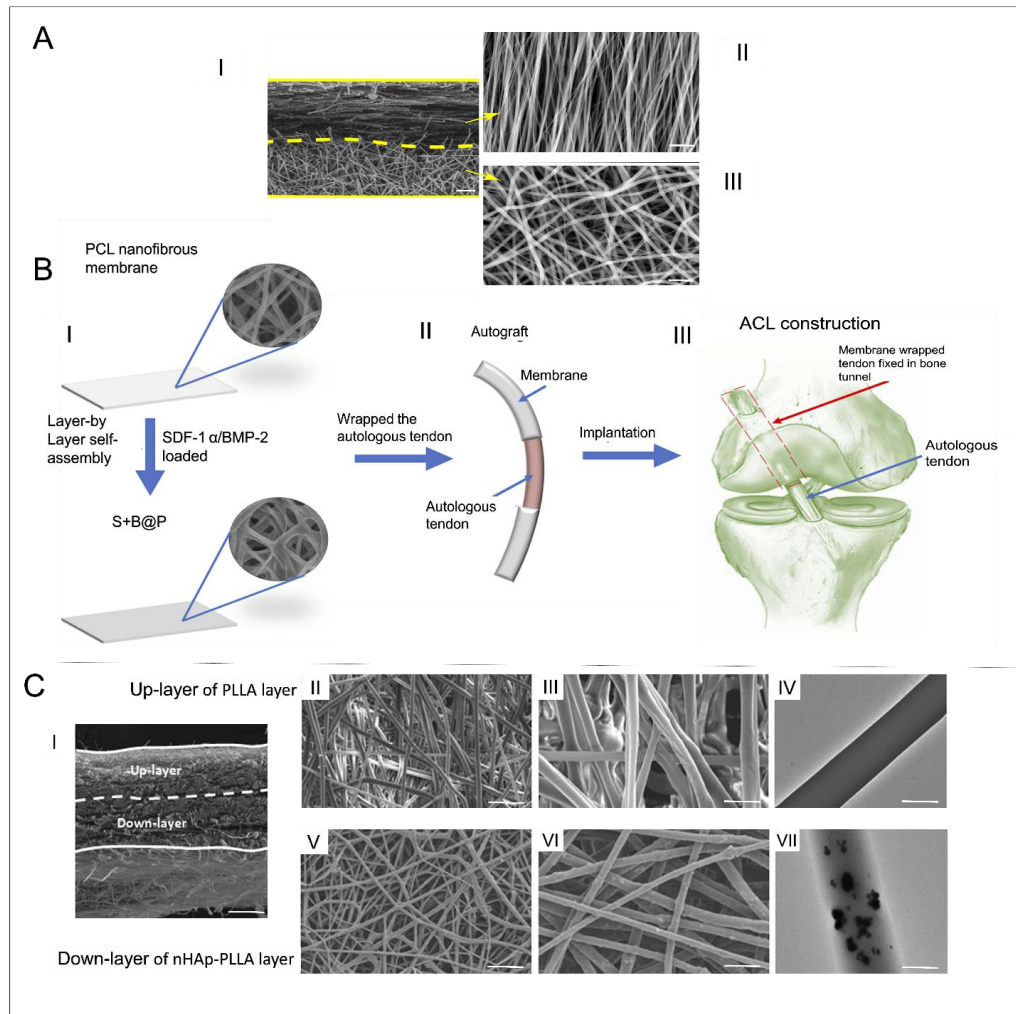
Figure 9. Multilayer images and applications. (A) SEM images of the dual layer aligned-random scaffold adapted from the Cai et al. study (Cai et al., 2018) : (I) cross section of the mesh (scale bar = 10 μm); (II) aligned region (scale bar = 5 μm); (III) random region (scale bar = 5 μm). (B) (I) Fabrication of the nanofibrous mat (II) Wrapping the autologous tendon with the membrane (III) Implantation of the graft; adapted from the Han et al. study (Han et al., 2019). (c) SEM images of the dual layer flexible nanofibrous membrane (BFM) in the Li et al. work (Li et al., 2017): (I) cross section of the membrane (scale bar = 100 μm); (II-III) upper layer of PLLA fibers (scale bar = 50 μm for (II) and 10 μm for (III)); (IV) TEM image of a PLLA fiber (scale bar = 1 μm); (V-VI) down layer of nHap-PLLA fibers (scale bar = 50 μm for (V) and 10 μm for (VII); TEM image of a nHap-PLLA fiber (scale bar = 1 μm)

Composites and 3D Structures

The complexity of the realized structures increased with the various attempts by scientists that starting from single mats and finally arrived to produce composites and 3D structures. These scaffolds were developed to try reproducing a biomimetic hierarchical organization of the nanofibers while producing gradients both along their length and thickness. A pioneering study in this field was done in the aforementioned research work of Samavedi et al., where they designed also a 3D structure with different regions in fiber orientation, diameter, mechanical and chemical properties (Samavedi et al., 2014). Starting from electrospun meshes, they cut them into pieces and rolled them around a guide, obtaining a sort of bundle with different nanofibers organizations (random PLGA at the extremities and axially aligned PCL in the central part). The 3D structures were mechanically evaluated by using a tensile test, showing that PCL10.5–PLGA13 had higher values of tensile moduli (3.2 ± 2.3MPa) compared to the PCL7.5-PLGA13 ones (2.6 ± 1.3 MPa). This dual drum setup allowed to obtain a 3D structures able to reproduce the nanofibers organization of the enthesis while maintaining the drum in rotation (Samavedi et al., 2014). In another work, Criscenti et al. fabricated an innovative triphasic scaffold for ligament-to-bone regeneration, combining a 3D printed reticular structure (3DP) and an electrospun mesh of aligned nanofibers (Criscenti et al., 2016) (Figure 10). Firstly, they produced the 3DP bone-inspired structure, and then they partially covered them with an electrospun aligned nanofiber membrane of PCL (tendon side) obtained with a gap collector strategy. In this way three different regions were obtained. The biomechanical tests revealed that the electrospun region had a failure stress of 5.21 ± 1.11 MPa and a stiffness of 88.9 ± 15.1 MPa, the 3DP region had instead a failure stress of 1.62 ± 0.27 MPa and a stiffness of 43.6 ± 8.1 MPa while the triphasic region had a failure stress of 2.57 ± 0.51 MPa and a stiffness of 50.6 ± 10.5 MPa. The mesenchymal stem cells cultures (hMSCs) revealed an higher proliferation in the electrospun region whereas an osteogenic differentiation was found to be higher in 3DP part while ligamentogenesis was found to be higher in the triphasic region (Criscenti et al., 2016). This inspiring methodology opened the way for the first time in the interfacial tissue engineering to match together the electrospinning and the additive manufacturing to reproduce the tissue gradients of the enthesis. Lin et al., with the aim of hierarchically organize their scaffold, realized a structure with a random-to-

aligned nanofibrous gradient to mimic the fiber arrangement at the ligament-bone insertion site (Lin et al., 2017). A solution of PCL was electrospun on a dual motor gap collector. The collector was composed of a pair of steel cones (random nanofibers) attached to the motor shafts with magnets with a gap between them (aligned nanofibers in the gap). At the end of the process a central bundle of aligned nanofibers with two conical random extremities was produced. The mechanical analysis revealed higher values of failure stress for the aligned region (38.7 ± 6.2 MPa) compared to the random one (6.3 ± 3.2 MPa). The biological tests carried out with human bone marrow mesenchymal stem cells (hBMSCs) revealed cell body elongation along the nanofibers direction of the aligned region, whereas they were randomly oriented inside the random region. The gene expression assay showed that tenogenic markers expression was significantly higher in the aligned region, while osteogenic markers expression was particularly intense in the random region (Lin et al., 2017). Spalazzi et al. with the purpose to induce enthesis fibrocartilage expression on ACL bovine specimens, covered by aligned nanofiber mats of PLGA, circular scaffolds of sintered nanospheres (Spalazzi et al., 2008) (Figure 10). The contraction of the simple nanofiber mesh revealed no significant differences between the control group and the scaffold one after 2 weeks while the contraction of the mesh+graft collar led to an increased matrix density and a distinct organization compared to the control group. Moreover after 2 weeks the control group kept its characteristic crimp while the mesh+graft collar retained its dense matrix pattern with no crimps and a high cellularity. In particular, they studied how the shrinkage of nanofibers could induce tendon matrix collagen distribution, cellularity, proteoglycan amount, and gene expression over 2 weeks. They found an upregulated expression of fibrocartilage-related markers such as type II collagen, aggrecan, and transforming growth factor-b3 (TGF-b3) (Spalazzi et al., 2008).
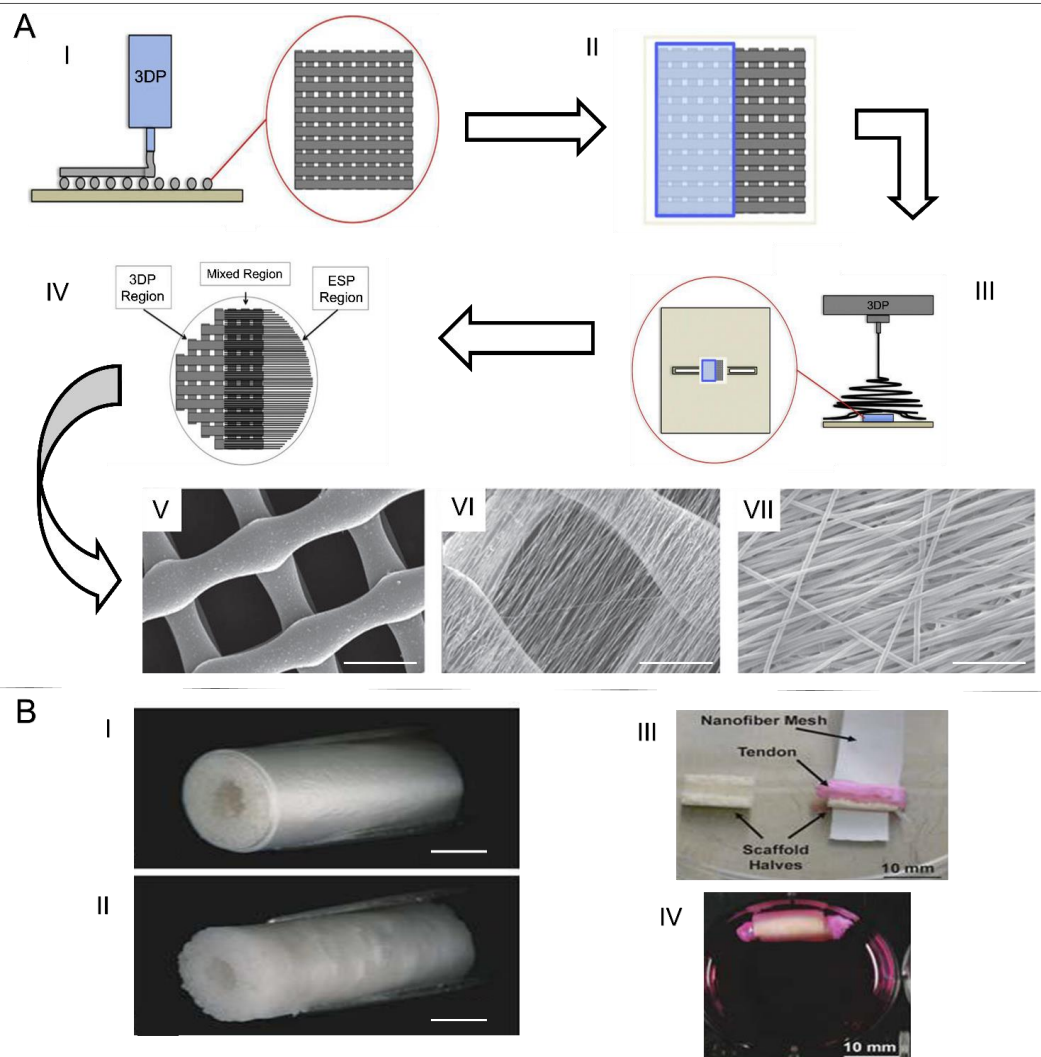
Figure 10. Composite structures. (a) The fabrication process adapted from the Criscenti et al. research work (Criscenti et al., 2016) : (I) Fabrication of the 3D printed PCL grid; (II) covering the 3DP scaffold with a paper foil; (III) Electrospinning of PLGA on the PCL grid; (IV) resulting mesh with 3 regions (3DP, mixed, ESP); (V-VII) SEM images of the regions ((V) 3DP region (scale bar = 500 μm); (VI) mixed region (scale bar = 200 μm); (VII) ESP region (scale bar = 20μm)). (b) The scaffold adapted from the Spalazzi et al. work (Spalazzi et al., 2008). (I) microspheres graft collar wrapped with the nanofiber mesh; (II) mesh+graft collar after 24 hours of mesh contraction; (III) tendon graft wrapped with the mesh and the graft collar; (IV) tendon graft wrapped with the mesh and the graft collar after 24 hours of contraction.

Table 5. Mechanical Properties

Test type	Tensile Modulus (MPa)	Load to Failure (N)	Failure Stress (MPa)	Failure Strain (%)	Applications	References
Uniaxial Tensile Test	From mineralized 120 down to 30			0% - 2% at 0.3 MPa 1% - 4% at 1.4 MPa 0% - 7% at 2.2 MPa	Tendon-to-Bone Interface	(Li et al., 2009)
Uniaxial Tensile Test	~ 75(Aligned) ~ 30(Random)		~ 45 (Aligned) ~ 20 (Random)		Tendon-to-Bone Interface	(Xie et al., 2010)
Uniaxial Tensile Test	4.490 ± 1.604 (PCL Side) 20.06 ± 7.773 (Center) 27.62 ± 6.063 (PLLA Side) 7.339 ± 2.131 (Whole Scaffold) 0.2789 ± 0.1509 (Native MTJ)		1.069 ± 0.2713 (PCL Side) 2.384 ± 0.5987 (Center) 3.741 ± 0.8486 (PLLA Side) 0.5058 ± 0.2130 (Whole) 0.1478 ± 0.01631 (Native MTJ)	130.4 ± 44.56 (PCL Side) 42.79 ± 17.75 (Center) 35.33 ± 8.964 (PLLA Side) 18.49 ± 8.210 (Whole) 122.4 ± 19.18 (Native MTJ)	Tendon-to-Bone Interface	(Ladd et al., 2011)
Uniaxial Tensile Test	* nHAP-PCL = 0.64 ± 0.04 GRAD = 0.58 ± 0.09 PEUUR2000 = 0.22 ± 0.03 ** nHAP-PCL = 2.4 ± 0.23 GRAD = 0.55 ± 0.01 PEUUR2000 = 0.23 ± 0.04 *Unmineralized **Mineralized		* nHAP-PCL = 0.2 GRAD = 0.5 PEUUR2000 = 0.6 ** nHAP-PCL = 0.45 GRAD = 0.4 PEUUR2000 = 0.6 *Unmineralized **Mineralized nHAP-PCL = 0.2 GRAD = 0,5 PEUUR2000 = 0.6 ** nHAP-PCL = 0.45 GRAD = 0.4 PEUUR2000 = 0.6 *Unmineralized **Mineralized	* nHAP-PCL = 45 ± 5 GRAD = 125 ± 25 PEUUR2000 = 165 ± 5 ** nHAP-PCL = 75 ± 25 GRAD = 125 PEUUR2000 = 250 *Unmineralized **Mineralized	Ligament-to-Bone Interface	(Samavedi et al., 2011)
Uniaxial Tensile Test	~560 (6 h) ~ 350 (2h) ~ 250 (0h) (Obtained by graphic)		Yield Stress ~ 5 (6h) ~ 6 (2h) ~ 7 (0h) (Obtained by graphic)		Tendon-to-Bone Interface	(Liu et al., 2011)

Test	Stiffness (N/mm)				Interface	Reference
Uniaxial Tensile Test	**Stiffness (N/mm)** Scaffold Reattachment * 1.3 ± 0.3 2.4 ± 0.3 ** 6.1 ± 2.2 7.3 ± 2.6 *** 12.8 ± 3.1 11.0 ± 3.1 **** 12.8 ± 3.1 10.2 ± 1.4 *0 Weeks **4 Weeks ***8 Weeks ****16 Weeks	Scaffold Reattachment * 5.4 ± 2.5 16.9 ± 6.0 ** 28.1 ± 12.0 61.7 ± 9.5 *** 71.7 ± 12.0 68.3 ± 21.5 **** 75.3 ± 18.7 69.4 ± 14.9 *0 Weeks **4 Weeks ***8 Weeks ****16 Weeks			Tendon-to-Bone Interface	(Inui et al., 2012)
Uniaxial Tensile Test	* 1650 ± 150 (Uniform circular) 1390 ± 100 (Non uniform) 2250 ± 250(Uniform ellipsoidal) ** 2490 ± 180 (Thick platelet) 1260 ± 230 (Thick Conformal) 1570 ± 170 (Thin Conformal) *Pristine PLGA **Mineralized PLGA		* 56 ± 3 (Uniform circular) 89 ± 7 (Non uniform) 145 ± 12 (Uniform ellipsoidal) ** 30 ± 4 (Thick platelet) 67 ± 0 (Thick Conformal) 136 ± 11 (Thin Conformal) *Pristine PLGA **Mineralized PLGA	* 150 ± 25 (Uniform circular) 122 ± 7 (Non uniform) 81 ± 7 (Uniform ellipsoidal) *Pristine PLGA	Tendon-to-Bone Interface	(Kolluru et al., 2013)
Monotonic Tensile Test	* Random(PLGA) 27.8 ± 7.9 Aligned(PCL) 6.8 ± 3.7 ** Random(PLGA) 23.8 ± 4.4 Aligned(PCL) 9.9 ±2.8 *PCL7.5-PLGA13 **PCL10.5-PLGA13		* Random (PLGA) 25 ± 9 Aligned (PCL) 50 ± 14 ** Random (PLGA) 24 ± 2 Aligned (PCL) 41 ± 12 *PCL7.5-PLGA13 **PCL10.5-PLGA13		Ligament-to-Bone Interface	(Samavedi et al., 2014)
Uniaxial Tensile Test	3100				Tendon-to-Bone Interface	(Lipner et al., 2014)

Uniaxial Tensile Test	**Stiffness (N/mm)** * 5.4 ± 0.6(Controls) 5.7 ± 0.7 (PLGA) 6.1 ± 0.6 (bFGF–PLGA) ** 7.9 ± 0.8 (Controls) 9.4 ± 0.8 (PLGA) 9.7 ± 0.5 (bFGF–PLGA) *** 13.0 ± 0.7 (Controls) 13.7 ± 0.7 (PLGA) 14.9 ± 0.3 (bFGF–PLGA) *2 Weeks **4 Weeks ***8 Weeks	* 8.3 ± 0.6 (Controls) 8.7 ± 0.9 (PLGA) 9.1 ± 0.9 (bFGF–PLGA) ** 18.2 ± 0.9 (Controls) 20.7±1.6 (PLGA) 21.4±1.3 (bFGF–PLGA) *** 27.1 ± 1.2 (Controls) 28.4 ± 1.2 (PLGA) 32.7 ± 1.0 (bFGF–PLGA) *2 Weeks **4 Weeks ***8 Weeks	* 1.00 ± 0.02 (Controls) 1.00 ± 0.02 (PLGA) 1.02±0.02 (bFGF–PLGA) ** 1.30±0.08 (Controls) 1.32 ± 0.06 (PLGA) 1.33 ± 0.05 (bFGF–PLGA) *** 1.65 ± 0.09 (Controls) 1.62 ± 0.03 (PLGA) 1.82 ± 0.03 (bFGF–PLGA) *2 Weeks **4 Weeks ***8 Weeks		Tendon-to-Bone Interface	(Zhao et al., 2014)
Uniaxial Tensile Test	**Stiffness (N/mm)** * ~ 5 (Control) ~ 5 (PLLA) ~ 5.5 (gelatin-PLLA) ** ~ 8.5 (Control) ~ 8.5 (PLLA) ~ 9.5 (gelatin-PLLA) *** ~ 13 (Control) ~ 13.5 (PLLA) ~ 14.5 (gelatin-PLLA) * 2 Weeks *4 Weeks *8 Weeks	* ~ 8 (Control) ~ 8 (PLLA) ~ 8 (gelatin-PLLA) ** ~ 19 (Control) ~ 20 (PLLA) ~ 21 (gelatin-PLLA) *** ~ 27 (Control)~ 28 (PLLA) ~ 31 (gelatin-PLLA) * 2 Weeks *4 Weeks *8 Weeks	* ~ 1.0 (Control) ~ 1.0 (PLLA) ~ 1.0 (gelatin-PLLA) ** ~ 1.3 (Control) ~ 1.3 (PLLA) ~ 1.4 (gelatin-PLLA) *** ~ 1.7 (Control) ~ 1.6 (PLLA) ~ 1.8 (gelatin-PLLA) * 2 Weeks *4 Weeks *8 Weeks		Tendon-to-Bone Interface	(Zhao et al., 2015)
Uniaxial Tensile Test	**Stiffness (N/mm)** * ~ 8.5 (PCL/nHAp/Col) ~ 7 (PCL) ** 15.2 ± 1.4 (PCL/nHAp/Col) 10.2 ± 1.3 (PCL) *4 weeks **8 weeks	* ~ 28 (PCL/nHAp/Col) ~ 25 (PCL) ** 58.4 ± 4.1 (PCL/nHAp/Col) 39.9 ± 3.4 (PCL) *4 weeks **8 weeks			Tendon-to-Bone Interface	(Han et al., 2015)

Uniaxial Tensile Test	* ~ 7 (Suture) ~ 7.5 (Acellular) ~ 6.5 (Cellular) ~ 4 (Cellular BMP2) ** ~ 13 (Suture) ~ 8 (Acellular) ~ 10 (Cellular) ~ 7.5 (Cellular BMP2) *28 days **56 days	* 21 ± 5.5 (Suture) 25 ± 5.9 (Acellular) 25.7 ± 9.4 (Cellular) 19.7 ± 5.9 (Cellular BMP2) ** 32.3 ± 4.9 (Suture) 31.1 ± 9.4 (Acellular) 31.7 ± 10 (Cellular) 32.6 ± 6.6 (Cellular BMP2) *28 days **56 days	* ~ 1.15 (Suture) ~ 1.4 (Acellular) ~ 1.4 (Cellular) ~ 0.75 (Cellular BMP2) ** ~ 2 (Suture) ~ 1.4 (Acellular) ~ 2 (Cellular) ~ 1.6 (Cellular BMP2) *28 days **56 days	* 34.14 ± 14 (Suture) 39 ± 29 (Acellular) 42 ± 11 (Cellular) 42 ± 16 (Cellular BMP2) ** 31.8 ± 8 (Suture) 34 ± 7 (Acellular) 38 ± 11 (Cellular) 50 ± 20 (Cellular BMP2) *28 days **56 days	Tendon-to-Bone Interface	(Lipner et al., 2015)
Uniaxial Tensile Test	**Stiffness (N/mm)** * ~ 6.5 (Control) ~ 7.5 (SF) ** ~ 9.5 (Control) ~ 14 (SF) *6 Weeks **12 Weeks	* ~ 31 (Control) ~ 40 (SF) ** ~ 51 (Control) ~ 67 (SF) *6 Weeks **12 Weeks			Tendon-to-Bone Interface	(Zhi et al., 2016)
Uniaxial Tensile Test	* 82.8 ± 11.6 ** 33.6 ± 14.8 *Aligned Region **Random region		* 38.7 ± 6.2 ** 6.3 ± 3.2 *Aligned Region **Random region	* 132.5 ± 26.4 ** 61.5 ± 13.3 *Aligned Region **Random region	Ligament-to-Bone Interface	(Lin et al., 2017)
Uniaxial Tensile Test	* 43.6 ± 8.1 ** 50.6 ± 10.5 *** 88.9 ± 15.1 *3DF **Mixed ***ESP		* 1.62 ± 0.27 ** 2.57 ± 0.51 *** 5.21 ± 1.11 *3DF **Mixed ***ESP	* 4.81 ± 0.69 ** 6.71 ± 0.31 *** 22.1 ± 3.2 *3DF **Mixed ***ESP	Ligament-to-Bone Interface	(Criscenti et al., 2016)

Test					Interface	Reference
Uniaxial Tensile Test		#* ~20 ##* ~ 20 #** ~ 41.4 (Average 37.4–44.5) ##** ~ 28.3 (Average 26.1–30.5) *8 Weeks **16 Weeks #With Nanofiber ##Without Nanofiber			Tendon-to-Bone Interface	(Chou et al., 2016)
Uniaxial Tensile Test	* ~ 1.8 (BPUR 10) ~ 7.5 (Transition) ~ 12.3 (BPUR 50) ** ~ 2 (BPUR 10) ~ 11 (Transition) ~ 17 (BPUR 50) *Random Gradient ** Aligned Gradient		* ~ 4.5 (BPUR 10) ~ 3 (Transition) ~ 3.5 (BPUR 50) ** ~ 4 (BPUR 10) ~ 3.8 (Transition) ~ 4 (BPUR 50) *Random Gradient ** Aligned Gradient	* ~ 210 (BPUR 10) ~ 160 (Transition) ~ 145 (BPUR 50) ** ~ 190 (BPUR 10) ~ 100 (Transition) ~ 75 (BPUR 50) *Random Gradient ** Aligned Gradient	Tendon-to-Bone Interface	(Kishan et al., 2017)
Uniaxial Tensile Test		* Nanofibrous Scaffolds 40N Micronanofibrous Scaffolds 200N ** Nanofibrous Scaffolds 100N Micronanofibrous Scaffolds 500N *Film Width 2 cm **Film Width 5cm			Ligament-to-Bone Interface	(He et al., 2017)

Uniaxial Tensile Test	**Stiffness (N/mm)** * ~ 11 (Control) ~ 11 (SFM) ~ 10.5 (BFM) ** ~ 13 (Control) ~ 13 (SFM) ~ 15 (BFM) *** ~ 13 (Control) ~ 16 (SFM) ~ 23 (BFM) * 4 weeks ** 8 weeks *** 12 weeks	* ~ 85 (Control) ~ 100 (SFM) ~ 75 (BFM) ** ~ 100 (Control) ~ 140 (SFM) ~ 160 (BFM) *** ~ 120 (Control) ~ 150 (SFM) ~ 180 (BFM) * 4 weeks ** 8 weeks *** 12 weeks	* ~ 3 (Control) ~ 3 (SFM) ~ 2.5 (BFM) ** ~ 3 (Control) ~ 3.5 (SFM) ~ 4 (BFM) *** ~ 3.5 (Control) ~ 3.8 (SFM) ~ 4.7 (BFM) * 4 weeks ** 8 weeks *** 12 weeks		Tendon-to-Bone Interface	(Li et al., 2017)
Uniaxial Tensile Test	* 21 (PCL600nm) 30 (PCL1000nm) 24 (PLA) 15 (PCL aligned) 32 (Blend PLA out) 60 (Blend PCL out) ** 20 (PCL 600nm) 36 (PCL 1000nm) 43 (PLA) 63 (PCL aligned) 30 (Blend PLA out) 38 (Blend PCL out) * Dry ** Wet				Tendon-to-Bone Interface	(Baudequin et al., 2017)
Uniaxial Tensile Test	**Stiffness (N/mm)** * 9.9 ± 1.9 (ARM) 9.3 ± 1.4 (RM) 5.8 ± 1.3 (Control) ** 21.5 ± 3.5 (ARM) 15.6 ± 1.6 (RM) 10.0 ± 1.1 (Control) *6 Weeks **12 Weeks	* 43.9 ± 7.5 (ARM) 41.4 ± 5.7 (RM) 25.3 ± 5.9 (Control) ** 83.2 ± 12.4 (ARM) 66.2 ± 6.6 (RM) 50.6 ± 3.5 (Control) *6 Weeks **12 Weeks			Tendon-to-Bone Interface	(Cai et al., 2018)

Uniaxial Tensile Test	215.5 (nHap-PCL/CS) 180 (PCL/CS)	250 (nHap-PCL/CS) 195 (PCL/CS)			Tendon-to-Bone Interface	(Wu et al., 2018)
Uniaxial Tensile Test	**Stiffness (N/mm)** * ~ 5 (PCL) ~ 7.5 (B@P) ~ 7 (S + B@P) ** 10.8 (PCL) 13.9 (B@P) 19.5 (S + B@P) * 6 weeks ** 12 weeks	* ~ 18 (PCL) ~ 30 (B@P) ~ 33 (S + B@P) ** 42.7 (PCL) 63.5 (B@P) 79.9 (S + B@P) * 6 weeks ** 12 weeks			Tendon-to-Bone Interface	(Han et al., 2019)
Uniaxial Tensile Test	17 (Obtained by graphic)		12 (Obtained by graphic)	70% (Obtained by graphic)	Tendon-to-Bone Interface	(Huang et al., 2019)
Uniaxial Tensile Test	**Stiffness (N/mm)** * ~ 5.5 (Control) ~ 5.5 (PCL) ~ 6.5 (Melatonin-PCL) ** ~ 7.5 (Control) ~ 7.5 (PCL) ~ 10 (Melatonin-PCL) *** ~ 11 (Control) ~ 13.5 (PCL) ~ 15.4 (Melatonin-PCL) * 2 weeks ** 4 weeks *** 8 weeks	* ~ 10 (Control) ~ 10 (PCL) ~ 10 (Melatonin-PCL) ** ~ 15 (Control) ~ 15 (PCL) ~ 20 (Melatonin-PCL) *** ~ 20 (Control) ~ 25 (PCL) ~ 33 (Melatonin-PCL) * 2 weeks ** 4 weeks *** 8 weeks	* ~ 1.2 (Control) ~ 1.2 (PCL) ~ 1 (Melatonin-PCL) ** ~ 1.6 (Control) ~ 1.5 (PCL) ~ 2.3 (Melatonin-PCL) *** ~ 2.1 (Control) ~ 2.7 (PCL) ~ 3.3 (Melatonin-PCL) * 2 weeks ** 4 weeks *** 8 weeks		Tendon-to-Bone Interface	(Song et al., 2019)

Uniaxial Tensile Test					Tendon-to-Bone Interface	(Zhu et al., 2019)
Uniaxial Tensile Test		* ~ 9 (Control) ~ 9.3 (PCL) ~ 9.7 (KGN-PCL) ** 15.3 ± 0.7 (Control) 19.4 ± 1.4 (PCL) 22.1 ± 0.5 (KGN-PCL) *** 20.7 ± 0.5 (Control) 25.5 ± 0.2 (PCL) 29.7 ± 1.6 (KGN-PCL) * 2 weeks ** 4 weeks *** 8 weeks			Tendon-to-Bone Interface	(Zhu et al., 2019)
Uniaxial Tensile Test	**Stiffness (N/mm)** * ~ 5.5 (Control) ~ 5.7 (PLGA) ~ 6.3 (GO-PLGA) ** ~ 8 (Control) ~ 8.2 (PLGA) ~ 9.8 (GO-PLGA) *** ~ 10 (Control) ~ 11.7 (PLGA) ~ 12.5 (GO-PLGA) * 4 weeks ** 8 weeks *** 12 weeks	* ~ 60 (Control) ~ 60 (PLGA) ~ 70 (GO-PLGA) ** ~ 90 (Control) ~ 95 (PLGA) ~ 115 (GO-PLGA) *** ~ 125 (Control) ~ 130 (PLGA) ~ 150 (GO-PLGA) * 4 weeks ** 8 weeks *** 12 weeks	* ~ 4.5 (Control) ~ 4.5 (PLGA) ~ 5.8 (GO-PLGA) ** ~ 5.3 (Control) ~ 5.8 (PLGA) ~ 6.5 (GO-PLGA) *** ~ 6.3 (Control) ~ 6.3 (PLGA) ~ 7.5 (GO-PLGA) * 4 weeks ** 8 weeks *** 12 weeks		Tendon-to-Bone Interface	(Su et al., 2019)
Uniaxial Tensile Test	**Stiffness (N/mm)** 7.74 ± 0.91 (CS–g–PCL) 8.06 ± 0.92 (TGF–β3–CS–g–PCL 12.46 ± 0.55 (Native enthesis)	15.7 ± 9.4 (CS–g–PCL) 23.2 ± 9.4 (TGF–β3–CS–g–PCL) 29.6 ± 7.9 (Native enthesis)			Tendon-to-Bone Interface	(Reifenrath et al., 2020)

Table 6. In vitro *cell culture*

Cell type	Time Point (Days)	Culture type	Applications	References
Mouse Preosteoblast Cells	3	Static	Tendon-to-Bone Interface	(Li et al., 2009)
Rat Tendon Fibroblasts	3-7	Static	Tendon-to-Bone Interface	(Xie et al., 2010)
C2C12 myoblasts	3-7	Static	Muscle-to-Tendon Interface	(Ladd et al., 2011)
NIH3T3 fibroblasts	3-7	Static	Muscle-to-Tendon Interface	(Ladd et al., 2011)
MC3T3-E1 osteoprogenitor cells	7	Static	Ligament-to-Bone Interface	(Samavedi et al., 2011)
MC3T3-E1 murine preosteoblasts	1-3-4-5-7-10	Static	Tendon-to-Bone Interface	(Han et al., 2015)
MC3T3-E1	2-6-10	Static	Ligament-to-Bone Interface	(He et al., 2017)
MC3T3-E1 Subclone 14	1 -3-5	Static	Tendon-to-Bone Interface	(Huang et al., 2019)
Rat Bone Marrow derived Stromal Cells (BMSCs)	1-7-14-21-28	Static	Ligament-to-Bone Interface	(Samavedi et al., 2012)
Rat Bone Marrow Mesenchymal Stem Cells	1-4-7	Static	Tendon-to-Bone Interface	(Zhu et al., 2019)
BMSCs	1-3-5-7-14-30	Static	Tendon-to-Bone Interface	(Han et al., 2019)
Rat Bone Marrow Mesenchymal Stem Cells	1-4-7-14-28	Static	Ligament-to-Bone Interface	(Jiang et al., 2020)
BMSCs	3	Static	Ligament-to-Bone Interface	(Samavedi et al., 2014)
C3H10T1/2 mouse fibroblasts	1-3-7	Static	Tendon-to-Bone Interface	(Zhao et al., 2015)
C3H10T1/2 (Mesenchymal stem cells model)	4	Static	Tendon-to-Bone Interface	(Baudequin et al., 2017)
Human dermal fibroblasts (HDFs)	1 -3-5	Static	Tendon-to-Bone Interface	(Zhao et al., 2014)
Human Adipose Derived Stem Cells (hADSCs)	3-7	Static	Tendon-to-Bone Interface	(Xie et al., 2012)
hADSCs	1-3-5-7	Static	Tendon-to-Bone Interface	(Perikamana et al., 2018)
Human Bone Marrow Mesenchymal stem cells (hBMSCs)	3	Static	Tendon-to-Bone Interface	(Kishan et al., 2017)
hBMSCs	1-3-5-7	Static	Ligament-to-Bone Interface	(Criscenti et al., 2016)
Human bone marrow mesenchymal stem cells	0-1-3-5-21	Static	Tendon-to-Bone Interface	(Song et al., 2019)
Human bone marrow mesenchymal stem cells (hBMSCs)	1-7-14-21	Static	Ligament-to-Bone Interface	(Lin et al., 2017)
Rabbit Bone Marrow Mesenchymal stem cells	1-3-5-7	Static	Tendon-to-Bone Interface	(Zhi et al., 2016)
Rabbit bone marrow mesenchymal stem cells	1-3-7-14	Static	Tendon-to-Bone Interface	(Su et al., 2019)
Bone marrow derived porcine Mesenchymal Stem Cells	0-10-20-21	Static	Ligament-to-Bone Interface	(Olvera et al., 2017)
Osteosarcoma (not specified)	1-4	Static	Tendon-to-Bone Interface	(Nowlin et al., 2018)
Fibroblasts (not specified)	1-4	Static	Tendon-to-Bone Interface	(Nowlin et al., 2018)
Human osteoblast cells (HOS)	2	Static	Tendon-to-Bone Interface	(Wu et al., 2018)
3 T3-L1	1 -3-5	Static	Tendon-to-Bone Interface	(Huang et al., 2019)
Rat tendon stem/progenitor cells (TSPCs)	1-3-4-5-7-14	Static	Tendon-to-Bone Interface	(Lin et al., 2019)

Table 7. In vivo *test*

Animal	Time Point (Weeks)	Surgical site	Applications	References
Rats				
144	2-4-8	Anterolateral aspect of the shoulder	Tendon-to-Bone Interface	(Zhao et al., 2015)
144	2-4-8	Anterolateral aspect of the shoulder	Tendon-to-Bone Interface	(Zhao et al., 2014)
144	2-4-8	Insertion site at the humerus	Tendon-to-Bone Interface	(Huang et al., 2019)
135	2-4-8	Anterolateral aspect of shoulder	Tendon-to-Bone Interface	(Zhu et al., 2019)
93	2-4-8	Anterolateral aspect of the shoulder	Tendon-to-Bone Interface	(Song et al., 2019)
17	8	Proximal part of the musculus triceps brachi (caput laterale)	Tendon-to-Bone Interface	(Reifenrath et al., 2020)
64	2-4-8	Humeral head	Tendon-to-Bone Interface	(Lipner et al., 2015)
Rabbits				
24	4-8	Bilateral limbs	Tendon-to-Bone Interface	(Han et al., 2015)
42	0-4-8-16	Greater tuberosity of the humeral head	Tendon-to-Bone Interface	(Inui et al., 2012)
32	6-12	Posterior ankle joint of right hindlimb	Tendon-to-Bone Interface	(Zhi et al., 2016)
48	8-16	Left knee joint	Tendon-to-Bone Interface	(Chou et al., 2016)
10	12	Left knee joint	Ligament-to-Bone Interface	(He et al., 2017)
144	4-8-12	Sopraspinatus Tendon insertion	Tendon-to-Bone Interface	(Li et al., 2017)
90	6-12	Achilles tendon of one hindlimb	Tendon-to-Bone Interface	(Cai et al., 2018)
48	4-8	Right knee joint	Tendon-to-Bone Interface	(Han et al., 2019)
108	4-8-12	Anterior superolateral approach for the shoulder joint	Tendon-to-Bone Interface	(Su et al., 2019)

5. Conclusions & Future Perspectives

The regeneration of the musculoskeletal interfaces represents one of the biggest challenges for the tissue engineering. Various techniques have been used trying to reach this goal and, among these, electrospinning has proved to be one of the most promising, primarily because its great versatility. Over the years and in particular in the last decades, different materials and designs have been used, obtaining increasingly encouraging results. Starting from simple mats, gradually more complex structures (biphasic, multilayer, composites, 3D) were proposed. These structures were often proposed as scaffolds to enhance cell proliferation for the regeneration of the musculoskeletal interfaces. The stimulation of these scaffolds with drugs and particles has also given very positive results in terms of cell differentiation. Despite these advances, an improvement of the mechanical properties is still needed, which are still inadequate for an implant in human patients. Besides, a major limitation of these works is the absence of long-term studies that investigate the efficiency of the scaffolds. So far, no hierarchical structures have been used, but thanks to recent advances in research a future perspective could see the use of hierarchical structures to approach the biomechanical properties of the original interface.

6. References

Abbasipour, M., and Khajavi, R. (2013). Nanofiber bundles and yarns production by electrospinning: A review. *Adv. Polym. Technol.* 32, 1–9. doi:10.1002/adv.21363.

Apostolakos, J., Durant, T. J. S., Dwyer, C. R., Russell, R. P., Weinreb, J. H., Alaee, F., et al. (2014). The enthesis: A review of the tendon-to-bone insertion. *Muscles. Ligaments Tendons J.* 4, 333–342. doi:10.11138/mltj/2014.4.3.333.

Arruda, E. M., Calve, S., Dennis, R. G., Mundy, K., and Baar, K. (2006). Regional variation of tibialis anterior tendon mechanics is lost following denervation. *J. Appl. Physiol.* 101, 1113–1117. doi:10.1152/japplphysiol.00612.2005.

Azizi, E., Halenda, G. M., and Roberts, T. J. (2009). Mechanical properties of the gastrocnemius aponeurosis in wild turkeys. *Integr. Comp. Biol.* 49, 51–58. doi:10.1093/icb/icp006.

Baldino, L., Cardea, S., Maffulli, N., and Reverchon, E. (2016). Regeneration techniques for bone-To-Tendon and muscle-To-Tendon interfaces reconstruction. *Br. Med. Bull.* 117, 25–37. doi:10.1093/bmb/ldv056.

Baldino, L., Maffulli, N., and Reverchon, E. (2015). *Bone-tendon interface*. Elsevier Ltd doi:10.1016/B978-1-78242-301-0.00014-8.

Baudequin, T., Gaut, L., Mueller, M., Huepkes, A., Glasmache, B., Duprez, D., et al. (2017). The osteogenic and tenogenic differentiation potential of C3H10T1/2 (mesenchymal stem cell model) cultured on PCL/PLA electrospun scaffolds in the absence of specific differentiation medium. *Materials (Basel).* 10, 1–19. doi:10.3390/ma10121387.

Bayrak, E., Ozcan, B., and Erisken, C. (2016). Processing of polycaprolactone and hydroxyapatite to fabricate graded electrospun composites for tendon-bone interface regeneration. *J. Polym. Eng.* 37, 99–106. doi:10.1515/polyeng-2016-0017.

Benjamin, M., Kumai, T., Milz, S., Boszczyk, B. M., Boszczyk, A. A., and Ralphs, J. R. (2002). The skeletal attachment of tendons - Tendon "entheses." *Comp. Biochem. Physiol. - A Mol. Integr. Physiol.* 133, 931–945. doi:10.1016/S1095-6433(02)00138-1.

Bhattarai, D. P., Aguilar, L. E., Park, C. H., and Kim, C. S. (2018). A review on properties of natural and synthetic based electrospun fibrous materials for bone tissue engineering. *Membranes (Basel).* 8. doi:10.3390/membranes8030062.

Bonnevie, E. D., and Mauck, R. L. (2018). Physiology and Engineering of the Graded Interfaces of Musculoskeletal Junctions. *Annu. Rev. Biomed. Eng.* 20, 403–429. doi:10.1146/annurev-bioeng-062117-121113.

Bosworth, L. A., and Downes, S. (2011). *Electrospinning for Tissue*

Regeneration. doi:10.1533/9780857092915.

Boys, A. J., McCorry, M. C., Rodeo, S., Bonassar, L. J., and Estroff, L. A. (2017). Next generation tissue engineering of orthopedic soft tissue-to-bone interfaces. *MRS Commun.* 7, 289–308. doi:10.1557/mrc.2017.91.

Cai, J., Wang, J., Ye, K., Li, D., Ai, C., Sheng, D., et al. (2018). Dual-layer aligned-random nanofibrous scaffolds for improving gradient microstructure of tendon-to-bone healing in a rabbit extra-articular model. *Int. J. Nanomedicine* 13, 3481–3492. doi:10.2147/IJN.S165633.

Calejo, I., Costa-Almeida, R., Reis, R. L., and Gomes, M. E. (2019). Enthesis Tissue Engineering: Biological Requirements Meet at the Interface. *Tissue Eng. - Part B Rev.* 25, 330–356. doi:10.1089/ten.teb.2018.0383.

Charvet, B., Ruggiero, F., and Le Guellec, D. (2012). The development of the myotendinous junction. A review. *Muscles. Ligaments Tendons J.* 2, 53–63.

Chen, J., Xu, J., Wang, A., and Zheng, M. (2009). Scaffolds for tendon and ligament repair: Review of the efficacy of commercial products. *Expert Rev. Med. Devices* 6, 61–73. doi:10.1586/17434440.6.1.61.

Chou, Y. C., Yeh, W. L., Chao, C. L., Hsu, Y. H., Yu, Y. H., Chen, J. K., et al. (2016). Enhancement of tendon–bone healing via the combination of biodegradable collagen-loaded nanofibrous membranes and a three-dimensional printed bone-anchoring bolt. *Int. J. Nanomedicine* 11, 4173–4186. doi:10.2147/IJN.S108939.

Criscenti, G., Longoni, A., Di Luca, A., De Maria, C., Van Blitterswijk, C. A., Vozzi, G., et al. (2016). Triphasic scaffolds for the regeneration of the bone-ligament interface. *Biofabrication* 8, 15009. doi:10.1088/1758-5090/8/1/015009.

Curzi, D., Ambrogini, P., Falcieri, E., and Burattini, S. (2013). Morphogenesis of rat myotendinous junction. *Muscles. Ligaments Tendons J.* 3, 275–280.

Dalton, P. D., Vaquette, C., Farrugia, B. L., Dargaville, T. R., Brown, T. D., and Hutmacher, D. W. (2013). Electrospinning and additive manufacturing: Converging technologies. *Biomater. Sci.* 1, 171–185. doi:10.1039/c2bm00039c.

Derwin, K. A., Galatz, L. M., Ratcliffe, A., and Thomopoulos, S. (2018). Enthesis Repair. *J. Bone Jt. Surg.* 100, e109. doi:10.2106/jbjs.18.00200.

Deymier, A. C., An, Y., Boyle, J. J., Schwartz, A. G., Birman, V., Genin, G. M., et al. (2017). Micro-mechanical properties of the tendon-to-bone attachment. *Acta Biomater.* 56, 25–35. doi:10.1016/j.actbio.2017.01.037.

Deymier, A. C., Schwartz, A. G., Cai, Z., Daulton, T. L., Pasteris, J. D., Genin, G. M., et al. (2019). The multiscale structural and mechanical effects of mouse supraspinatus muscle unloading on the mature enthesis. *Acta Biomater.* 83, 302–313. doi:10.1016/j.actbio.2018.10.024.

Deymier, A. C., Schwartz, A. G., Lim, C., Wingender, B., Kotiya, A., Shen, H., et al. (2020). Multiscale effects of spaceflight on murine tendon and bone. *Bone* 131. doi:10.1016/j.bone.2019.115152.

Font Tellado, S., Balmayor, E. R., and Van Griensven, M. (2015). Strategies to engineer tendon/ligament-to-bone interface: Biomaterials, cells and growth factors. *Adv. Drug Deliv. Rev.* 94, 126–140. doi:10.1016/j.addr.2015.03.004.

Frontera, W. R., and Ochala, J. (2015). Skeletal Muscle: A Brief Review of Structure and Function. *Behav. Genet.* 45, 183–195. doi:10.1007/s00223-014-9915-y.

Fung, Y. C. (1993). *Biomechanics: Mechanical Properties of Living Tissues*.

Genin, G. M., Kent, A., Birman, V., Wopenka, B., Pasteris, J. D., Marquez, P. J., et al. (2009). Functional grading of mineral and collagen in the attachment of tendon to bone. *Biophys. J.* 97, 976–985. doi:10.1016/j.bpj.2009.05.043.

Gotti, C., Sensini, A., Carloni, R., Zucchelli, A., and Focarete, M. L. (2020a). Hierarchical fibrous structures for muscle-inspired soft-actuators: a review. *Appl. Mater. Today*.

Gotti, C., Sensini, A., Fornaia, G., Gualandi, C., Zucchelli, A., and Focarete, M. L. (2020b). Biomimetic Hierarchically Arranged Nanofibrous Structures Resembling the Architecture and the Passive Mechanical Properties of Skeletal Muscles: A Step Forward Toward Artificial Muscle. *Front. Bioeng. Biotechnol.* 8, 1–22. doi:10.3389/fbioe.2020.00767.

Grove, DPM, J. R. (2008). Autograft, Allograft and Xenograft Options in the Treatment of Neglected Achilles Tendon Ruptures: A Historical Review with Illustration of Surgical Repair. *Foot Ankle J.* 1. doi:10.3827/faoj.2008.0105.0001.

Haider, A., Haider, S., and Kang, I. K. (2018). A comprehensive review summarizing the effect of electrospinning parameters and potential applications of nanofibers in biomedical and biotechnology. *Arab. J. Chem.* 11, 1165–1188. doi:10.1016/j.arabjc.2015.11.015.

Halpern, W., and Moss, R. L. (1976). Elastic modulus and stress relationships in stretched and shortened frog sartorii. *Am. J. Physiol.* 230, 205–210. doi:10.1152/ajplegacy.1976.230.1.205.

Han, F., Chen, T., and Lin, C. (2019). A LbL-Assembled Bioactive Coating Modi fi ed Nano fi brous Membrane for Rapid Tendon-Bone Healing in ACL Reconstruction. *Int. J. Nanomedicine* 2019:14, 9159–9172.

Han, F., Zhang, P., Sun, Y., Lin, C., Zhao, P., and Chen, J. (2015). Hydroxyapatite-doped polycaprolactone nanofiber membrane improves tendon–bone interface healing for anterior cruciate ligament reconstruction. *Int. J. Nanomedicine* 10, 7333–7343. doi:10.2147/IJN.S92099.

He, J., Jiang, N., Qin, T., Zhang, W., Liu, Z., Liu, Y., et al. (2017). Microfiber-reinforced nanofibrous scaffolds with structural and material gradients to mimic ligament-to-bone interface. *J. Mater. Chem. B* 5, 8579–8590. doi:10.1039/c7tb02089a.

He, J., Qin, T., Liu, Y., Li, X., Li, D., and Jin, Z. (2014). Electrospinning of nanofibrous scaffolds with continuous structure and material gradients. *Mater. Lett.* 137, 393–397. doi:10.1016/j.matlet.2014.09.045.

Huang, K., Su, W., Zhang, X., Chen, C., Zhao, S., Yan, X., et al. (2019). Cowpea-

like bi-lineage nanofiber mat for repairing chronic rotator cuff tear and inhibiting fatty infiltration. *Chem. Eng. J.* doi:10.1016/j.cej.2019.123671.

Inui, A., Kokubu, T., Mifune, Y., Sakata, R., Nishimoto, H., Nishida, K., et al. (2012). Regeneration of rotator cuff tear using electrospun poly(d,l-Lactide-Co- Glycolide) scaffolds in a rabbit model. *Arthrosc. - J. Arthrosc. Relat. Surg.* 28, 1790–1799. doi:10.1016/j.arthro.2012.05.887.

Jang, J. H., Castano, O., and Kim, H. W. (2009). Electrospun materials as potential platforms for bone tissue engineering. *Adv. Drug Deliv. Rev.* 61, 1065–1083. doi:10.1016/j.addr.2009.07.008.

Jiang, N., He, J., Zhang, W., Li, D., and Lv, Y. (2020). Directed differentiation of BMSCs on structural/compositional gradient nanofibrous scaffolds for ligament-bone osteointegration. *Mater. Sci. Eng. C* 110. doi:10.1016/j.msec.2020.110711.

Kannus, P. (2000). Structure of the tendon connective tissue. *Scand. J. Med. Sci. Sport.* 10, 312–320. doi:10.1034/j.1600-0838.2000.010006312.x.

Kastelic, J., Galeski, A., and Baer, E. (1978). The multicomposite structure of tendon. *Connect. Tissue Res.* 6, 11–23. doi:10.3109/03008207809152283.

Kishan, A. P., Robbins, A. B., Mohiuddin, S. F., Jiang, M., Moreno, M. R., and Cosgriff-Hernandez, E. M. (2017). Fabrication of macromolecular gradients in aligned fiber scaffolds using a combination of in-line blending and air-gap electrospinning. *Acta Biomater.* 56, 118–128. doi:10.1016/j.actbio.2016.12.041.

Kolluru, P. V., Lipner, J., Liu, W., Xia, Y., Thomopoulos, S., Genin, G. M., et al. (2013). Strong and tough mineralized PLGA nanofibers for tendon-to-bone scaffolds. *Acta Biomater.* 9, 9442–9450. doi:10.1016/j.actbio.2013.07.042.

Kopperdahl, D. L., and Keaveny, T. M. (1998). Yield strain behavior of trabecular bone. *J. Biomech.* 31, 601–608. doi:10.1016/S0021-9290(98)00057-8.

Kostrominova, T. Y., Calve, S., Arruda, E. M., and Larkin, L. M. (2009). Ultrastructure of myotendinous junctions in tendon-skeletal muscle constructs engineered in vitro. *Histol. Histopathol.* 24, 541–550. doi:10.14670/HH-24.541.

Kuthe, C. D., and Uddanwadiker, R. V. (2016). Investigation of effect of fiber orientation on mechanical behavior of skeletal muscle. *J. Appl. Biomater. Funct. Mater.* 14, e154–e162. doi:10.5301/jabfm.5000275.

Ladd, M. R., Lee, S. J., Stitzel, J. D., Atala, A., and Yoo, J. J. (2011). Co-electrospun dual scaffolding system with potential for muscle-tendon junction tissue engineering. *Biomaterials* 32, 1549–1559. doi:10.1016/j.biomaterials.2010.10.038.

Lännergren, J. (1971). The effect of low-level activation on the mechanical properties of isolated frog muscle fibers. *J. Gen. Physiol.* 58, 145–162. doi:10.1085/jgp.58.2.145.

Li, X., Cheng, R., Sun, Z., Su, W., Pan, G., Zhao, S., et al. (2017). *Flexible bipolar nanofibrous membranes for improving gradient microstructure in tendon-to-bone healing.* doi:10.1016/j.actbio.2017.07.044.

Li, X., Xie, J., Lipner, J., Yuan, X., Thomopoulos, S., and Xia, Y. (2009). Nanofiber scaffolds with gradations in mineral content for mimicking the tendon-to-bone insertion site. *Nano Lett.* 9, 2763–2768. doi:10.1021/nl901582f.

Light, N., and Champion, A. E. (1984). Characterization of muscle epimysium, perimysium and endomysium collagens. *Biochem. J.* 219, 1017–1026. doi:10.1042/bj2191017.

Lin, Y., Zhang, L., Liu, N. Q., Yao, Q., Handel, B. Van, Xu, Y., et al. (2019). In vitro behavior of tendon stem/progenitor cells on bioactive electrospun nanofiber membranes for tendon-bone tissue engineering applications. *Int. J. Nanomedicine* 14, 5831–5848. doi:10.2147/IJN.S210509.

Lin, Z., Zhao, X., Chen, S., and Du, C. (2017). Osteogenic and tenogenic induction of hBMSCs by an integrated nanofibrous scaffold with chemical and structural mimicry of the bone-ligament connection. *J. Mater. Chem. B* 5, 1015–1027. doi:10.1039/c6tb02156e.

Lipner, J., Liu, W., Liu, Y., Boyle, J., Genin, G. M., Xia, Y., et al. (2014). The mechanics of PLGA nanofiber scaffolds with biomimetic gradients in mineral for tendon-to-bone repair. *J. Mech. Behav. Biomed. Mater.* 40, 59–68. doi:10.1016/j.jmbbm.2014.08.002.

Lipner, J., Shen, H., Cavinatto, L., Liu, W., Havlioglu, N., Xia, Y., et al. (2015). In Vivo Evaluation of Adipose-Derived Stromal Cells Delivered with a Nanofiber Scaffold for Tendon-to-Bone Repair. *Tissue Eng. - Part A* 21, 2766–2774. doi:10.1089/ten.tea.2015.0101.

Liu, W., Yeh, Y. C., Lipner, J., Xie, J., Sung, H. W., Thomopoulos, S., et al. (2011). Enhancing the stiffness of electrospun nanofiber scaffolds with a controlled surface coating and mineralization. *Langmuir* 27, 9088–9093. doi:10.1021/la2018105.

Loh, Q. L., and Choong, C. (2013). Three-dimensional scaffolds for tissue engineering applications: Role of porosity and pore size. *Tissue Eng. - Part B Rev.* 19, 485–502. doi:10.1089/ten.teb.2012.0437.

Madhurapantula, R. S., Eidsmore, A., Modrich, C. D., and Orgel, J. P. R. O. (2017). New Methodology and Preliminary Data in the Charac-terization of the Muscle Tendon Junction of Mammalian Muscle Tissues. *EMS Eng. Sci. J.* 1, 7.

Maganaris, C. N., and Narici, M. V. (2005). Mechanical properties of tendons. *Tendon Inj. Basic Sci. Clin. Med.*, 14–21. doi:10.1007/1-84628-050-8_2.

Mirzaali, M. J., Schwiedrzik, J. J., Thaiwichai, S., Best, J. P., Michler, J., Zysset, P. K., et al. (2016). Mechanical properties of cortical bone and their relationships with age, gender, composition and microindentation properties in the elderly. *Bone* 93, 196–211. doi:10.1016/j.bone.2015.11.018.

Mo, X. M., Xu, C. Y., Kotaki, M., and Ramakrishna, S. (2004). Electrospun P(LLA-CL) nanofiber: A biomimetic extracellular matrix for smooth muscle cell and endothelial cell proliferation. *Biomaterials* 25, 1883–1890. doi:10.1016/j.biomaterials.2003.08.042.

Morgan, E. F., Unnikrisnan, G. U., and Hussein, A. I. (2018). Bone Mechanical Properties in Healthy and Diseased States. *Annu. Rev. Biomed. Eng.* 20, 119–143. doi:10.1146/annurev-bioeng-062117-121139.

Moss, R. L., and Halpern, W. (1977). Elastic and viscous properties of resting frog skeletal muscle. *Biophys. J.* 17, 213–228. doi:10.1016/S0006-3495(77)85651-8.

Murphy, W., Black, J., and Hastings, G. (2016). *Handbook of Biomaterial Properties, Second Edition*. doi:10.1007/978-1-4939-3305-1_11.

Nowlin, J., Bismi, M. A., Delpech, B., Dumas, P., Zhou, Y., and Tan, G. Z. (2018). Engineering the hard–soft tissue interface with random-to-aligned nanofiber scaffolds. *Nanobiomedicine* 5, 1–9. doi:10.1177/1849543518803538.

Nukavarapu, S., Freeman, J. W., and Laurencin, C. T. (2015). *Biomaterials and scaffolds for musculoskeletal tissue engineering*. doi:10.1016/B978-1-78242-301-0.00001-X.

O'Brien, F. J. (2011). Biomaterials & scaffolds for tissue engineering. *Mater. Today* 14, 88–95. doi:10.1016/S1369-7021(11)70058-X.

O'Connor, R. A., and McGuinness, G. B. (2016). Electrospun nanofibre bundles and yarns for tissue engineering applications: A review. *Proc. Inst. Mech. Eng. Part H J. Eng. Med.* 230, 987–998. doi:10.1177/0954411916656664.

Oftadeh, R., Perez-Viloria, M., Villa-Camacho, J. C., Vaziri, A., and Nazarian, A. (2015). Biomechanics and Mechanobiology of Trabecular Bone: A Review. *J. Biomech. Eng.* 137, 1–15. doi:10.1115/1.4029176.

Olvera, D., Sathy, B. N., Carroll, S. F., and Kelly, D. J. (2017). Modulating microfibrillar alignment and growth factor stimulation to regulate mesenchymal stem cell differentiation. *Acta Biomater.* 64, 148–160. doi:10.1016/j.actbio.2017.10.010.

Olvera, D., Sathy, B. N., and Kelly, D. J. (2020). Tissue Engineering and Regenerative Medicine Spatial presentation of tissue-specific extracellular matrix components along electrospun scaffolds for tissue engineering the bone-ligament interface. doi:10.1021/acsbiomaterials.0c00337.

Palmer, E., Kuong, S. J., and Elmadbouh, H. M. (1999). MR Imaging of Myotendinous Strain. *Am. J. Roentgenol.*, 703–709.

Patel, S., Caldwell, J. M., Doty, S. B., Levine, W. N., Rodeo, S., Soslowsky, L. J., et al. (2018). Integrating soft and hard tissues via interface tissue engineering. *J. Orthop. Res.* 36, 1069–1077. doi:10.1002/jor.23810.

Perikamana, S., Lee, J., Ahmad, T., Kim, E. M., Byun, H., Lee, S., et al. (2018). Harnessing biochemical and structural cues for tenogenic differentiation of adipose derived stem cells (ADSCs) and development of an in vitro tissue interface mimicking tendon-bone insertion graft. *Biomaterials* 165, 79–93. doi:10.1016/j.biomaterials.2018.02.046.

Po-Yee Lui, P., Zhang, P., Chang, K.-M., and Qin, L. (2010). Biology and augmentation of tendon-bone insertion repair. *J. Orthop. Surg. Res.* 5, 1–14. doi:10.1186/1749-799X-5-59.

Ramachandran, K., and Gouma, P.-I. (2008). Electrospinning for bone tissue engineering. *Recent Pat. Nanotechnol.* 2, 1–7. doi:10.2174/187221008783478608.

Ramakrishna, S., Fujihara, K., Teo, W. E., Lim, T. C., and Ma, Z. (2005). *An introduction to electrospinning and nanofibers*. doi:10.1142/5894.

Ramakrishna, S., Fujihara, K., Teo, W. E., Yong, T., Ma, Z., and Ramaseshan, R. (2006). Electrospun nanofibers: Solving global issues. *Mater. Today* 9, 40–50. doi:10.1016/S1369-7021(06)71389-X.

Reifenrath, J., Wellmann, M., Kempfert, M., Angrisani, N., Welke, B., Gniesmer, S., et al. (2020). TGF–β3 loaded electrospun polycaprolacton fibre scaffolds for rotator cuff tear repair: An in vivo study in rats. *Int. J. Mol. Sci.* 21. doi:10.3390/ijms21031046.

Reilly, D. T., and Burstein, A. H. (1975). The elastic and ultimate properties of compact bone tissue. *J. Biomech.* 8. doi:10.1016/0021-9290(75)90075-5.

Rho, J. Y., Kuhn-Spearing, L., and Zioupos, P. (1998). Mechanical properties and the hierarchical structure of bone. *Med. Eng. Phys.* 20, 92–102. doi:10.1016/S1350-4533(98)00007-1.

Robertson, A., Nutton, R. W., and Keating, J. F. (2006). Current trends in the use of tendon allografts in orthopaedic surgery. *J. Bone Jt. Surg. - Ser. B* 88, 988–992. doi:10.1302/0301-620X.88B8.17555.

Røhl, L., Larsen, E., Linde, F., Odgaard, A., and Jørgensen, J. (1991). Tensile and compressive properties of cancellous bone. *J. Biomech.* 24, 1143–1149. doi:10.1016/0021-9290(91)90006-9.

Rossetti, L., Kuntz, L. A., Kunold, E., Schock, J., Müller, K. W., Grabmayr, H., et al. (2017). The microstructure and micromechanics of the tendon-bone insertion. *Nat. Mater.* 16, 664–670. doi:10.1038/nmat4863.

Rothrauff, B. B., Lauro, B. B., Yang, G., Debski, R. E., Musahl, V., and Tuan, R. S. (2017). Braided and Stacked Electrospun Nanofibrous Scaffolds for Tendon and Ligament Tissue Engineering. *Tissue Eng. - Part A* 23, 378–389. doi:10.1089/ten.tea.2016.0319.

Samavedi, S., Guelcher, S. A., Goldstein, A. S., and Whittington, A. R. (2012). Response of bone marrow stromal cells to graded co-electrospun scaffolds and its implications for engineering the ligament-bone interface. *Biomaterials* 33, 7727–7735. doi:10.1016/j.biomaterials.2012.07.008.

Samavedi, S., Olsen Horton, C., Guelcher, S. A., Goldstein, A. S., and Whittington, A. R. (2011). Fabrication of a model continuously graded co-electrospun mesh for regeneration of the ligament-bone interface. *Acta Biomater.* 7, 4131–4138. doi:10.1016/j.actbio.2011.07.008.

Samavedi, S., Vaidya, P., Gaddam, P., Whittington, A. R., and Goldstein, A. S. (2014). Electrospun meshes possessing region-wise differences in fiber orientation, diameter, chemistry and mechanical properties for engineering bone-ligament-bone tissues. *Biotechnol. Bioeng.* 111, 2549–2559. doi:10.1002/bit.25299.

Santos, M. L. ., Rodrigues, M. T., Domingues, R. M. A., Reis, R. L., and Gomes,

M. . (2017). Regenerative Strategies for the Treatment of Knee Joint Disabilities. *Stud. Mechanobiol. Tissue Eng. Biomater.*, 349–371. doi:10.1007/978-3-319-44785-8.

Schleifenbaum, S., Schmidt, M., Möbius, R., Wolfskämpf, T., Schröder, C., Grunert, R., et al. (2016). Load and failure behavior of human muscle samples in the context of proximal femur replacement. *BMC Musculoskelet. Disord.* 17, 1–7. doi:10.1186/s12891-016-0998-7.

Sensini, A., and Cristofolini, L. (2018). Biofabrication of electrospun scaffolds for the regeneration of tendons and ligaments. *Materials (Basel).* 11, 1–43. doi:10.3390/ma11101963.

Sensini, A., Gualandi, C., Focarete, M. L., Belcari, J., Zucchelli, A., Boyle, L., et al. (2019). Multiscale hierarchical bioresorbable scaffolds for the regeneration of tendons and ligaments. *Biofabrication* 11, 035026. doi:10.1088/1758-5090/ab20ad.

Smith, C. W., Young, I. S., and Kearney, J. N. (1996). Mechanical properties of tendons: Changes with sterilization and preservation. *J. Biomech. Eng.* 118, 56–61. doi:10.1115/1.2795946.

Smith, L., Xia, Y., Galatz, L. M., Genin, G. M., and Thomopoulos, S. (2012). Tissue-engineering strategies for the tendon/ligament-to-bone insertion. *Connect. Tissue Res.* 53, 95–105. doi:10.3109/03008207.2011.650804.

Song, W., Ma, Z., Wang, C., Li, H., and He, Y. (2019). Pro-chondrogenic and immunomodulatory melatonin-loaded electrospun membranes for tendon-to-bone healing. *J. Mater. Chem. B* 7, 6564–6575. doi:10.1039/c9tb01516g.

Spalazzi, J. P., Vyner, M. C., Jacobs, M. T., Moffat, K. L., and Lu, H. H. (2008). Mechanoactive scaffold induces tendon remodeling and expression of fibrocartilage markers. *Clin. Orthop. Relat. Res.* 466, 1938–1948. doi:10.1007/s11999-008-0310-8.

Speer, K. P., Lohnes, J., Garrett, W. E., and Eriksson, E. (1993). Radiographic imaging of muscle strain injury. *Am. J. Sports Med.* 21, 89–96. doi:10.1177/036354659302100116.

Su, W., Wang, Z., Jiang, J., Liu, X., Zhao, J., and Zhang, Z. (2019). Promoting tendon to bone integration using graphene oxide-doped electrospun poly(lactic-co-glycolic acid) nanofibrous membrane. *Int. J. Nanomedicine* 14, 1835–1847. doi:10.2147/IJN.S183842.

Sung, H. J., Meredith, C., Johnson, C., and Galis, Z. S. (2004). The effect of scaffold degradation rate on three-dimensional cell growth and angiogenesis. *Biomaterials* 25, 5735–5742. doi:10.1016/j.biomaterials.2004.01.066.

Taneja, A. K., Kattapuram, S. V., Chang, C. Y., Simeone, F. J., Bredella, M. A., and Torriani, M. (2014). MRI findings of rotator cuff myotendinous junction injury. *Am. J. Roentgenol.* 203, 406–411. doi:10.2214/AJR.13.11474.

Tidball, J. G. (1991). 12 Myotendinous Junction Injury in Relation to Junction structure and molecular composition.pdf. 419–446.

Tidball, J. G., O'Halloran, T., and Burridge, K. (1986). Talin at myotendinous junctions. *J. Cell Biol.* 103, 1465–1472. doi:10.1083/jcb.103.4.1465.

Turner, C. E. (2000). Paxillin and focal adhesion signalling. *Nat. Cell Biol.* 2, 231–236. doi:10.1038/35046659.

VanDusen, K. W., and Larkin, L. M. (2015). *Muscle-tendon interface*. Elsevier Ltd doi:10.1016/B978-1-78242-301-0.00017-3.

Vang, P. (2006). Advantages and disadvantages between allograft versus autograft in anterior cruciate ligament replacement. *Significance*, 82–83.

Wang, J. H. C. (2006). Mechanobiology of tendon. *J. Biomech.* 39, 1563–1582. doi:10.1016/j.jbiomech.2005.05.011.

Weiner, S., and Traub, W. (1992). Bone structure: from ångstroms to microns. *FASEB J.* 6, 879–885. doi:10.1096/fasebj.6.3.1740237.

Weiner, S., and Wagner, H. D. (1998). The material bone: Structure-mechanical function relations. *Annu. Rev. Mater. Sci.* 28, 271–298. doi:10.1146/annurev.matsci.28.1.271.

Wu, G., Deng, X., Song, J., and Chen, F. (2018). Enhanced biological properties of biomimetic apatite fabricated polycaprolactone/chitosan nanofibrous bio-composite for tendon and ligament regeneration. *J. Photochem. Photobiol. B Biol.* 178, 27–32. doi:10.1016/j.jphotobiol.2017.10.011.

Xie, J., Li, X., Lipner, J., Manning, C. N., Schwartz, A. G., Thomopoulos, S., et al. (2010). "Aligned-to-random" nanofiber scaffolds for mimicking the structure of the tendon-to-bone insertion site. *Nanoscale* 2, 923–926. doi:10.1039/c0nr00192a.

Xie, J., Ma, B., Michael, P. L., and Shuler, F. D. (2012). Fabrication of Nanofiber Scaffolds With Gradations in Fiber Organization and Their Potential Applications. *Macromol. Biosci.* 12, 1336–1341. doi:10.1002/mabi.201200115.

Yamamoto, A., Takagishi, K., Osawa, T., Yanagawa, T., Nakajima, D., Shitara, H., et al. (2010). Prevalence and risk factors of a rotator cuff tear in the general population. *J. Shoulder Elb. Surg.* 19, 116–120. doi:10.1016/j.jse.2009.04.006.

Yang, P. J., and Temenoff, J. S. (2009). Engineering orthopedic tissue interfaces. *Tissue Eng. - Part B Rev.* 15, 127–141. doi:10.1089/ten.teb.2008.0371.

Z. Paxton, J. (2013). Current Progress in Enthesis Repair: Strategies for Interfacial Tissue Engineering. *Orthop. Muscular Syst.* 01, 1–13. doi:10.4172/2161-0533.s1-003.

Zhang, X., Bogdanowicz, D., Erisken, C., Lee, N. M., and Lu, H. H. (2012). Biomimetic scaffold design for functional and integrative tendon repair. *J. Shoulder Elb. Surg.* 21, 266–277. doi:10.1016/j.jse.2011.11.016.

Zhao, C., Wang, S., Wang, G., Su, M., Song, L., Chen, J., et al. (2018). Preparation of decellularized biphasic hierarchical myotendinous junction extracellular matrix for muscle regeneration. *Acta Biomater.* 68, 15–28. doi:10.1016/j.actbio.2017.12.035.

Zhao, S., Xie, X., Pan, G., Shen, P., Zhao, J., and Cui, W. (2015). Healing improvement after rotator cuff repair using gelatin-grafted poly(L-lactide)

electrospun fibrous membranes. *J. Surg. Res.* 193, 33–42. doi:10.1016/j.jss.2014.08.019.

Zhao, S., Zhao, J., Dong, S., Huangfu, X., Li, B., Yang, H., et al. (2014). Biological augmentation of rotator cuff repair using bFGF-loaded electrospun poly(lactide-co-glycolide) fbrous membranes. *Int. J. Nanomedicine* 9, 2373–2385. doi:10.2147/IJN.S59536.

Zhi, Y., Liu, W., Zhang, P., Jiang, J., and Chen, S. (2016). Electrospun silk fibroin mat enhances tendon-bone healing in a rabbit extra-articular model. *Biotechnol. Lett.* 38, 1827–1835. doi:10.1007/s10529-016-2158-4.

Zhu, Q., Ma, Z., Li, H., Wang, H., and He, Y. (2019). Enhancement of rotator cuff tendon-bone healing using combined aligned electrospun fibrous membranes and kartogenin. *RSC Adv.* 9, 15582–15592. doi:10.1039/c8ra09849b.